

Observation of suppressed viscosity in the normal state of ^3He due to superfluid fluctuations

Rakin N. Baten¹, Yefan Tian¹, Eric N. Smith¹, Erich J. Mueller¹, Jeevak M. Parpia^{1*}

¹*Department of Physics, Cornell University, Ithaca, N.Y. 14853, USA*

**jmp9@cornell.edu*

August 29, 2023

Abstract:

By monitoring the quality factor of a quartz tuning fork oscillator we have observed a fluctuation-driven reduction in the viscosity of bulk ^3He in the normal state near the superfluid transition temperature, T_c . These fluctuations, which are only found within $100\mu\text{K}$ of T_c , play a vital role in the theoretical modeling of ordering; they encode details about the Fermi liquid parameters, pairing symmetry, and scattering phase shifts. They will be of crucial importance for transport probes of the topologically nontrivial features of superfluid ^3He under strong confinement. Here we characterize the temperature and pressure dependence of the fluctuation signature, finding data collapse consistent with the predicted theoretical behavior.

Introduction

The normal state of a superfluid contains transient ordered patches which grow as the system is cooled towards the transition temperature T_c . Observing the influence of these fluctuations on transport in liquid ^3He has been a scientific goal which has been unfulfilled for nearly 50 years¹. Similar fluctuations are found near other ordered states, such as magnets², superconductors³, and alkali gases⁴, where they are often related to pseudogap phenomena^{5,6}. These fluctuations have been particularly well studied in ^4He , where the extremely short coherence length allows the λ anomaly in the heat capacity of ^4He to serve as a model system for scaling⁷. Due to the low pairing energy and long coherence length, finding such signatures in ^3He , however, has been challenging. Here we observe a fluctuation induced suppression of the viscosity of bulk ^3He near T_c . This provides crucial information about the transport signature which can be used to probe contemporary phenomena such as the topologically nontrivial nature of superfluidity in confined ^3He ⁸.

The low temperature normal state of ^3He is our best example of a Fermi liquid, whose properties are understood in terms of a gas of interacting quasiparticles⁹. As the temperature is lowered, the phase space available for scattering is reduced and the mean time between scattering events grows as $\tau \propto T^{-2}$. As a consequence, transverse momentum gradients produce smaller stresses at low temperatures, quantified by the viscosity $\eta \propto \tau \propto T^{-2}$. A scattering resonance emerges as the liquid is cooled towards the superfluid transition, where particles form short-lived Cooper pairs during scattering events. Such resonances enhance the scattering, leading to a decrease in

the viscosity. In a clean 3D system (such as ^3He), this suppression occurs in only a very narrow window of temperature $\delta T = T - T_c$ where the pair lifetime $\tau_{\text{GL}} \approx \hbar/k_B\delta T$ is comparable to τ . Thus one only expects to see a measurable reduction of the viscosity at temperatures of order 1% above T_c . In principle the nature of these fluctuations will change when one is within the scaling regime^{10,11} $\delta T/T_c = (T_c/T_F)^4 \approx 10^{-12}$, but in practice such precision is unachievable.

In addition to being of fundamental interest, the fluctuation contributions to transport are important for future experiments which will look for edge modes¹²⁻¹⁴ in ^3He as a signature of topological superfluidity¹⁵⁻²⁰. The contribution to viscosity from these edge modes will be small, and accurate measurements will be needed to distinguish them from the effects of fluctuations. Here we report the necessary base-line measurements.

Fluctuation effects in ^3He have previously been observed in the attenuation of zero (collisionless) sound²¹⁻²³, with ever increasing experimental and theoretical sophistication²⁴⁻²⁷. While valuable, these are not a substitute for transport experiments. Observing the fluctuation contributions to viscosity is challenging and previous attempts²⁸⁻³¹ have had flaws which obscured or complicated the phenomena. In this work we overcome these challenges.

Firstly, Refs. 30,31 observed significant deviation from Fermi-liquid behavior ($\eta \propto T^{-2}$) at all temperatures. Such deviations are unphysical, and are not seen in heat capacity⁵, thermal conductivity³³, in collisionless sound measurements²¹, or in previous measurements with quartz forks³⁴. The deviations may be due to the temperature dependence of the properties of the metallic alloys used as vibrating elements⁸. We avoid this issue by using quartz forks.

Secondly, Refs. 28, 29 inferred temperature from the susceptibility of a small sample of undiluted Cerous Magnesium Nitrate (CMN). While accurate at $\sim 10\text{mK}$, this approach suffers from systematic errors near the magnetic ordering temperature of CMN. Our current experiment uses a Lanthanum Diluted Cerous Magnesium Nitrate thermometer (Figure 1a), referencing thermometry to the widely accepted PLTS2000 temperature scale^{3,37}.

Finally, our experiment takes pains to work within the hydrodynamic regime, where the viscous mean free path λ_η is small compared to all other relevant length-scales. In Refs. 28, 29, λ_η was comparable to the cavity height at low pressure, leading to slip, and deviations from Fermi-liquid behavior which obscured the influence of fluctuations. Torsional oscillator experiments³⁸ find that the contributions from these Knudsen effects become observable when the device dimensions are $d \approx 8\lambda_\eta$. In the present work, our fork has tines which are 0.61 mm wide \times 0.253 mm thick \times 3.64 mm long, spaced 0.194 mm apart, housed in a cylindrical casing ≈ 3 mm in diameter (Figure 1b). The smallest of these dimensions, the 0.194 mm tine spacing, is more than 8 times λ_η except at the very lowest temperatures (see Supplemental Note 1, Supplemental Table 1). Thus, Knudsen effects should be negligible.

Results

We monitor the quality factor $Q = f_0/\Delta f$ of a quartz fork³⁴ immersed in liquid ^3He cooled to mK temperatures by a nuclear demagnetization stage³⁹. Here, f_0 is the resonant frequency and Δf is the resonance linewidth. The oscillator damping can be related to the helium viscosity

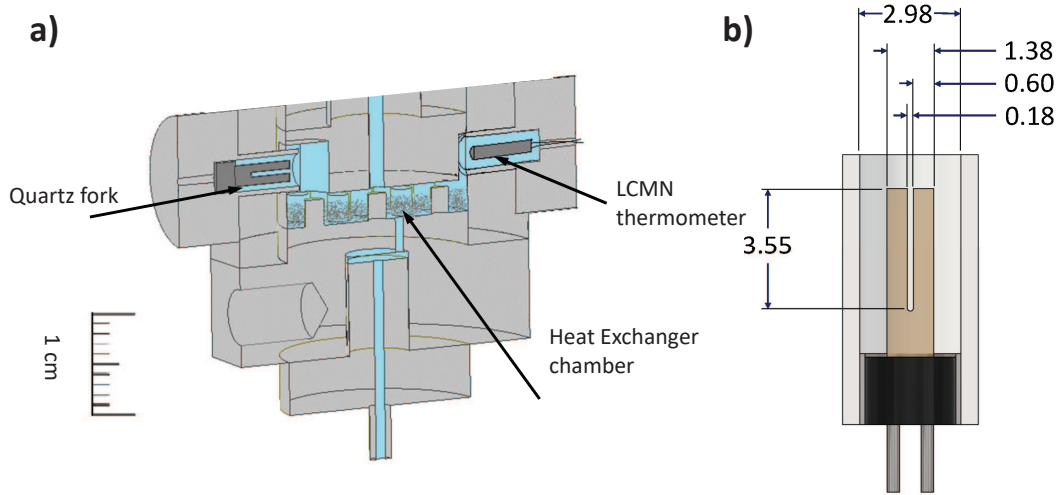


Figure 1: **Cell Schematic** a) The location of the quartz fork and LCMN thermometer are shown in relation to the heat exchanger. b) Schematic image of the quartz fork with dimensions in millimeters.

$(Q \propto \eta^{-1/2})^{34}$, and we operate in the hydrodynamic regime. Temperature was measured with a diluted paramagnetic salt thermometer placed in the same ^3He volume proximate to the quartz fork. Additional details on thermometry, fork operation, Fermi liquid viscosity, the hydrodynamic regime and background subtraction are provided in the methods section and in Supplementary Notes 1 and 2. The pressure was maintained at a constant value using electronic feedback for each temperature sweep.

The data obtained at several pressures from 0.5 bar to 29.3 bar are shown in Figure 2 a). For each data set we show the best linear fit as a dashed line passing through the origin, corresponding to the Fermi liquid prediction $\eta \propto T^{-2}$ (ie. $Q \propto T$). In Figure 2 b), we compare the value of Q/T obtained at all pressures near T_c , illustrating the extent of the departure from Fermi liquid behavior near T_c .

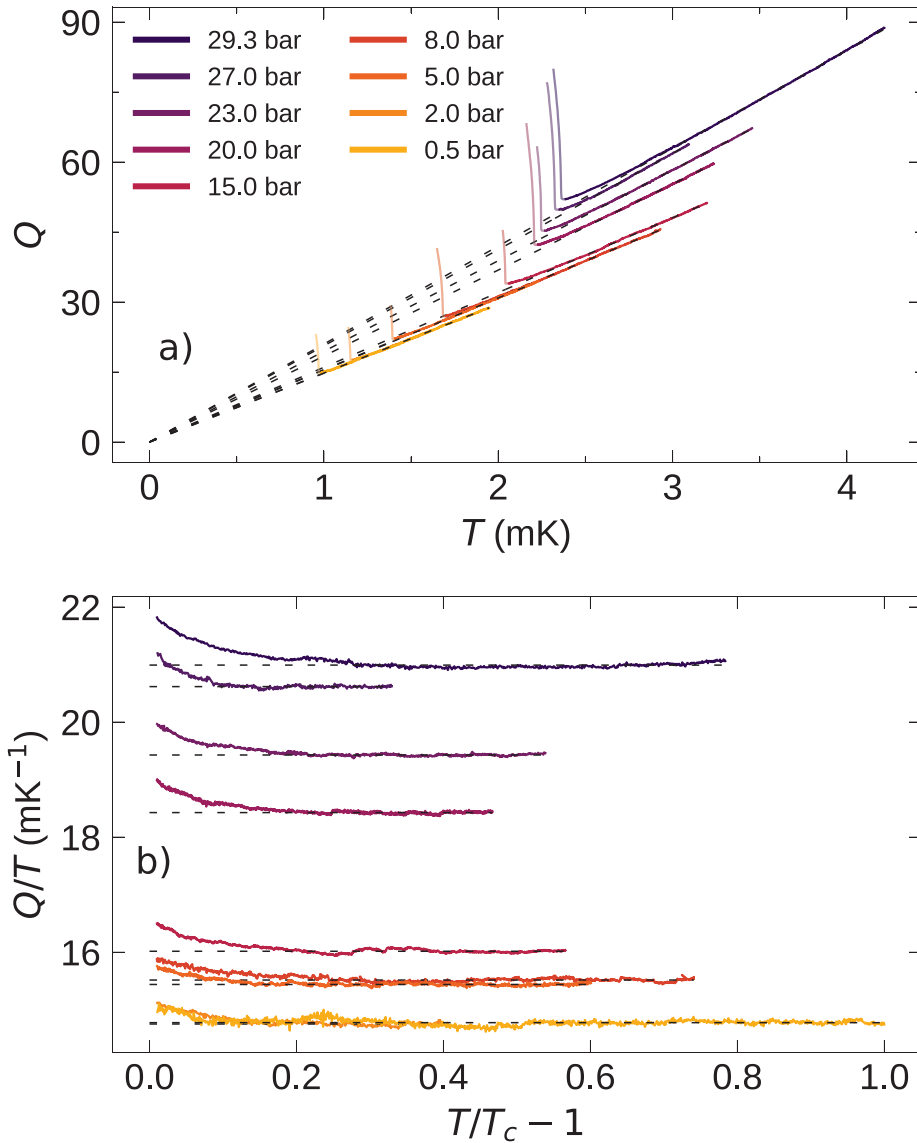


Figure 2: **Quartz Fork Q vs Temperature** a) The inferred Q of the quartz fork at various pressures vs the temperature. The expected Fermi liquid behavior was obtained after processing described in Supplementary Note 2, ($Q \propto \eta^{-1/2} \propto T$), and is represented by dashed lines. The superfluid transition is marked by an abrupt increase in the Q , and data below T_c is shown as lighter shaded lines. b) Plot of Q/T vs $(1 - T/T_c)$. This plot illustrates the extent of the departure of Q from linear behavior with pressure.

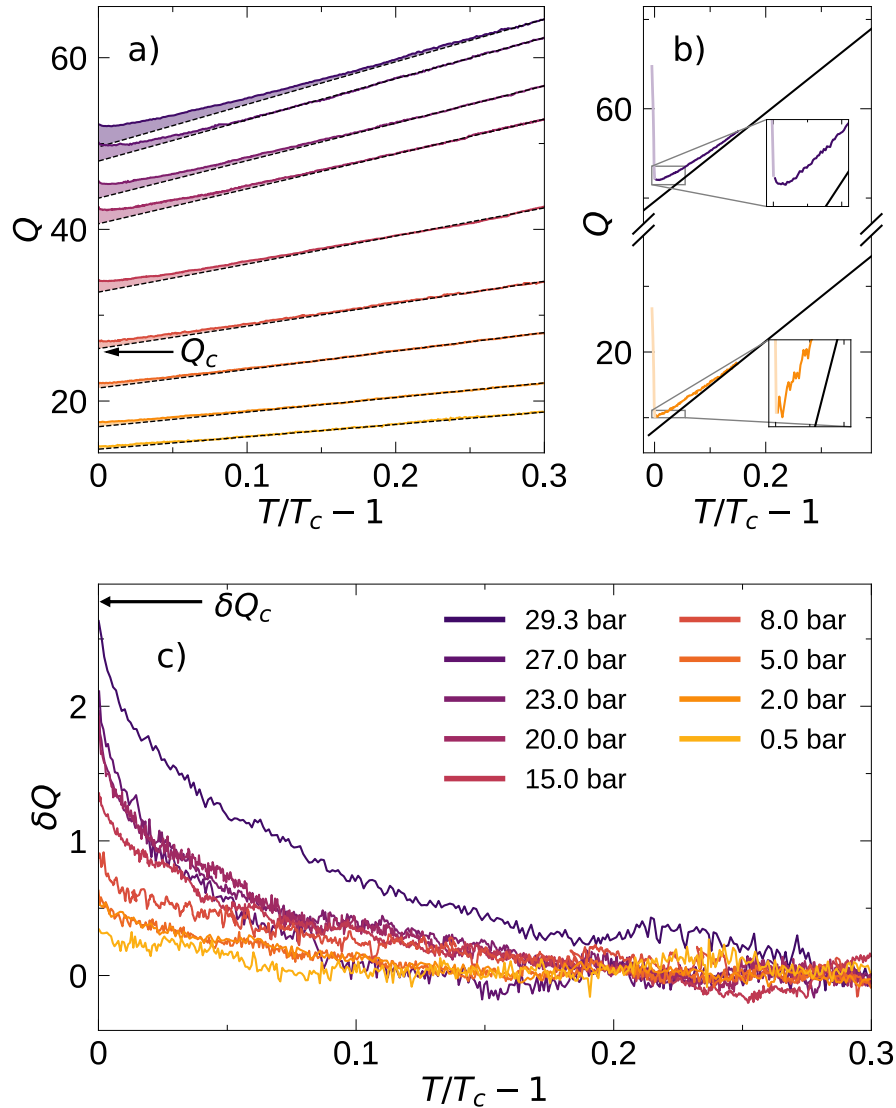


Figure 3: **Quartz Fork Q vs Temperature near T_c** a) Departure from the Fermi liquid behavior (linear slope) is seen at all pressures just above T_c . Also marked is the value of Q_c for the 8 bar run. b) Q vs $(T/T_c - 1)$ near T_c of the 29.3 bar and 2 bar runs. It is evident from the insets that the higher pressure run shows a minimum in the Q before T_c is attained, while the lower pressure data shows no minimum. c) The excess Q vs $T/T_c - 1$.

As T_c is approached from above (Figure 3a)), a small increase in Q (δQ) is observed relative to the dashed line, corresponding to a suppression of η . At high pressure, the deviations are large enough that Q actually passes through a minimum in the normal state. At low pressure, δQ is smaller, though it can be resolved. The differences between high and low pressure results are highlighted in Figure 3 b) and its insets. Upon entering in to the superfluid state the Q sharply increases due to the rapid decrease in viscosity^{28,40-42} at T_c . The quality of the data is sufficient to illustrate the development of δQ in Figure 3 c) with pressure.

Discussion

Proximity to superfluidity enhances quasiparticle scattering: Quasiparticles that pass near each other form short-lived pairs, increasing the scattering rate, $1/\tau$. The viscosity is proportional to the scattering time τ , ($\propto T^{-2}$), which is therefore suppressed near T_c . Emery¹ writes the fluctuation contribution to the viscous scattering time τ as

$$\frac{\delta\tau}{\tau} = -\Gamma \left(\frac{k_B T_F \tau}{\hbar} \right) (k_F \xi_{00})^{-3} \alpha \left(1 - \frac{\theta^{1/2}}{\alpha} \tan^{-1} \frac{\alpha}{\theta^{1/2}} \right) \quad (1)$$

where the quantity $\delta\tau$ is the additional scattering time due to the broken pairs above T_c , and α is a fitting constant. Here $\theta = \frac{T}{T_c} - 1$ is the reduced temperature, T_F is the Fermi temperature, and Γ is a numerical constant that depends on the pairing and the transport parameter (in this case viscosity, η). The unitless quantity $k_F \xi_{00}$ is the product of the Fermi wavevector and the pairing coherence

length, and in bulk ^3He can be expressed as

$$(k_F \xi_{00})^2 = \frac{7\zeta(3)}{12\pi^2} \left(\frac{T_F}{T_c} \right)^2 \quad (2)$$

where $\zeta(3) \approx 1.2$ is Apéry's constant and ζ is the Riemann Zeta function.

Since the $Q \propto \eta^{-1/2} \propto \tau^{-1/2}$, it follows that $\delta Q/Q = -1/2 \delta\tau/\tau$. We can rewrite $\tau(T) = \tau_c \times (T_c/T)^2$ and $Q(T) = Q_c \times T/T_c$. Q_c is the value of the Q at T_c without the contribution due to fluctuations (See Figure 3b)). Thus $(\delta\tau/\tau) = -2 (\delta Q/Q_c) \times (T_c/T)$. This yields a modified version of Equation (1),

$$\frac{\delta Q(T)}{Q_c} = C(P) \frac{\alpha}{1 + \theta} \left(1 - \frac{\theta^{1/2}}{\alpha} \tan^{-1} \frac{\alpha}{\theta^{1/2}} \right), \quad (3)$$

and

$$C(P) = \frac{1}{2} \Gamma \left(\frac{k_B T_F \tau_c}{\hbar} \right) (k_F \xi_{00})^{-3}. \quad (4)$$

We can extract Q_c from the linear fits in Figure 3 and plot the ratio $\delta Q/Q_c$ from Eq. (3) in Figure 4 a). For small θ , Eq. (3) has the form $\delta Q \approx \delta Q_c (1 - \pi\theta^{1/2}/2\alpha)$, where δQ_c is the excess Q at T_c . Thus, it is natural to use $\theta^{1/2}$ as the horizontal axis. Both Q_c and δQ increase with pressure, but δQ has a slightly stronger dependence: The ratio $\delta Q_c/Q_c$ varies from $\sim 2\%$ at the lowest pressure measured to $\sim 5\%$ at the highest. The corresponding values of the zero sound attenuation coefficient, A , $\delta A/A_c$ measured in collisionless sound varied from $\sim 8\%$ at 32.56 bar, $\sim 6.5\%$ at 19.94 bar and “very approximately $\sim 2\%$ ” at 0.05 bar²¹. Assuming that α is not pressure

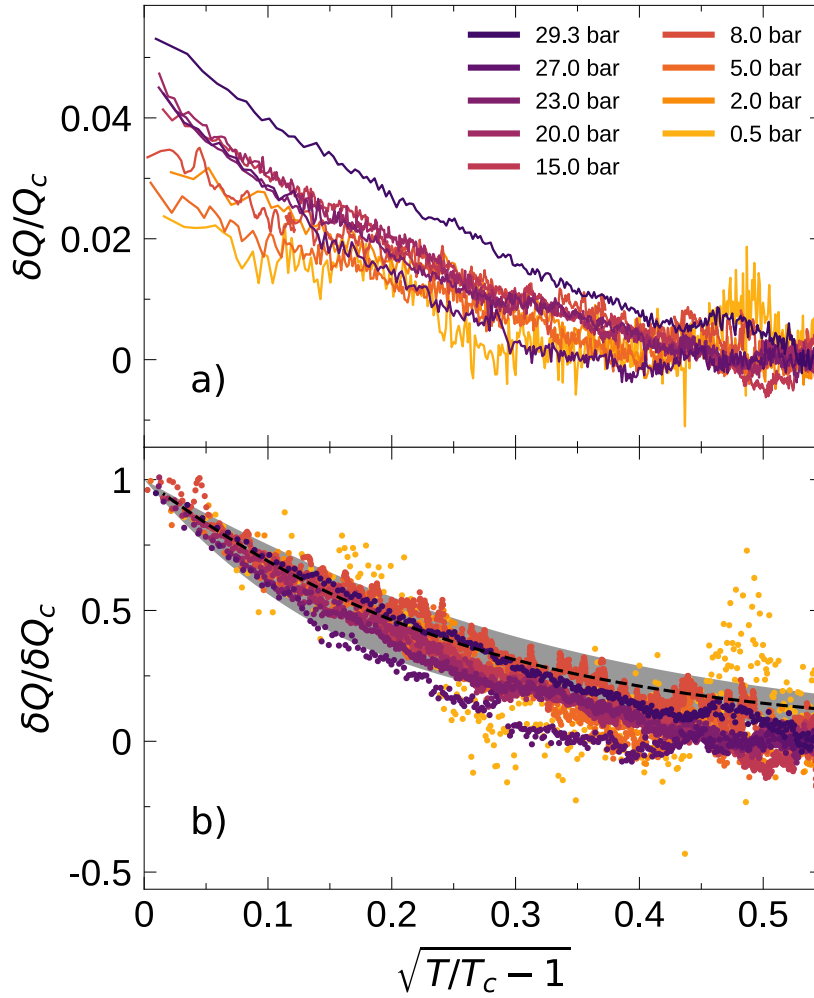


Figure 4: **Normalized fluctuation contribution vs reduced temperature** a) The measured excess Q (see Figure 3) of the quartz fork at various pressures, normalized to Q_c (see Figure 3 c)) plotted against the square root of reduced temperature. This plot shows that the contribution to Q of the fluctuation component increases faster than the increase of Q_c with pressure. b) δQ normalized to δQ_c (see Eqs. 3, 4). The dashed line shows the expected temperature dependent fit to the fluctuation component of viscosity in Eq. (1) (see Ref [1]). The shaded gray region represents the 1σ range in the curve fit based upon the error in the fit parameters.

dependent, Eq. (3) predicts that the excess Q 's should collapse if normalized as $\delta Q/\delta Q_c$. In Figure 4 b) we test that feature, showing Emery's prediction as a black dashed line, using $\alpha = 0.43$. The agreement is quite remarkable, with slight deviations at larger values of $\theta^{1/2}$.

We further quantify this agreement by independently fitting each fixed-pressure run to Eq. (3), extracting our best estimates of the pressure dependence of $\delta Q_c = C(P)\alpha Q_c$ and α . As seen in Figure 5 a), any pressure dependence of α is weak. The contributions to $C(P)$ in Eq. (4) are reasonably well known. We take ηT^2 from Ref [2] to calculate τ_c (after correction for temperature scales), and v_F , n and m^*/m from Ref [5, 6]; (See Supplementary Note 1 for more details). Emery argues that $19.5 < \Gamma < 46.8$ for p wave pairing, with the true value likely lying in the middle of that range. We treat Γ as a free parameter, finding a best-fit value $\Gamma = 40.8$, which is at the upper end of the expected range. Nonetheless, the resulting curve, shown in Fig. 5 b), agrees very well with our measurements. The error bars on α , $\delta Q_c/Q$ in Figure 5 a), b) represent a 1σ standard deviation. The error bars on α are derived from the calculation of the fit to Equation 3 and random noise error in Q ; the error bars on $\delta Q_c/Q_c$ in Figure 5 b) are derived from the error in δQ_c (the error in Q_c is negligible in comparison to δQ_c).

The somewhat large value of Γ may be the result of limitations in Emery's modeling. Lin and Sauls²⁷ argued that Emery's calculation contains some double-counting, and that it incorrectly included interference terms among the different scattering channels. Another source of theoretical uncertainty is the scattering time τ which we used in evaluating Eq. (4). In any event, the magnitudes of the fluctuation contribution to the viscosity are seen to be smaller than the values noted in

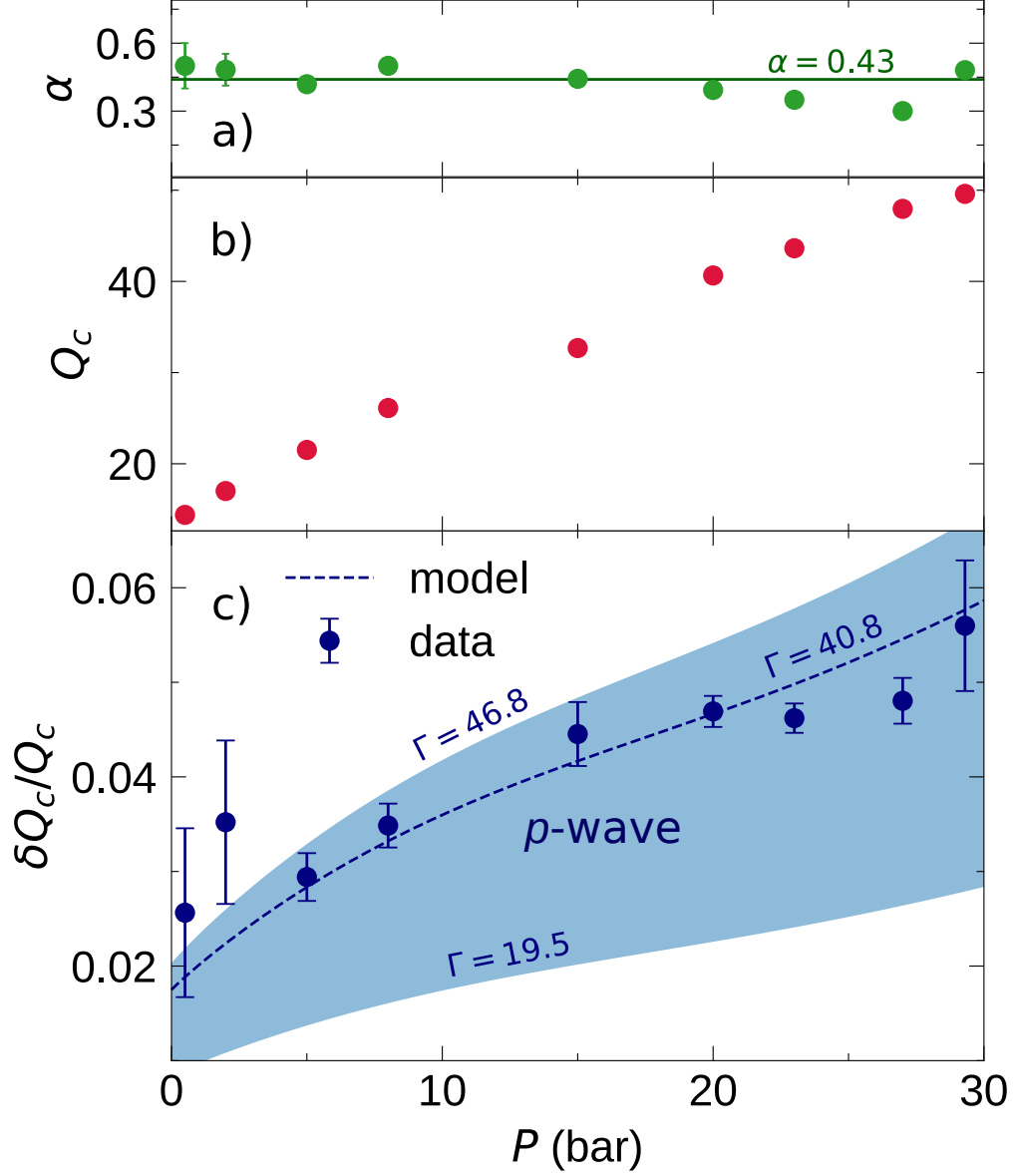


Figure 5: **Comparison of measured and calculated parameters** **a)** The values of α obtained to yield the fit shown in Figure 4 b). The horizontal line denotes the mean α . **b)** Values of Q_c based on the linear fits for Fermi liquid behavior shown in Figure 3. **c)** δQ_c , normalized by Q_c plotted against the pressure. The dashed line shows the expected temperature dependent fit to the normalized fluctuation component in Eq. 3 (see Ref [1]) based on previously measured values of ηT^2 (Ref [2]), v_F , n and m^*/m (Ref [5, 6]). Details in Supplementary Note 1, Supplementary Table 1. Shaded blue region marks the variation of Γ for p wave pairing in the model by Emery (Ref [1]).

References [21, 22].

With improvements in signal recovery using low temperature amplifiers, the precision and noise of the excess Q could be greatly improved, and perhaps used to measure the pressure dependence of the Landau parameter F_2^s as was proposed for collisionless sound²⁷. The values of F_2^s are poorly known²⁷, as they are derived from the pressure dependence of the attenuation of transverse zero sound which a difficult to measure parameter⁴⁵.

Looking forward, an important next step will be to extend these measurements to strongly confined geometries, where topological surface states appear^{12–20}. In such geometries T_c can be significantly suppressed¹⁸, leaving an extended region where fluctuations can potentially become stronger. Experiments studying thermal transport in such narrow channels¹⁹ reveal a crossover between bulk and surface dominated regimes, which depend on surface quality^{18,46,47}. The role of pairing fluctuations, and their interaction with surface modes, has not yet been established, and will be the focus of future research. For the present study conducted in bulk ^3He , the impact of surface states (that exist only below T_c) on fluctuations should be negligible.

We have observed that incipient pairing fluctuations contribute a small but significant portion of the scattering above T_c . This contribution is resolved at all pressures, and is comparable to that observed using the attenuation of collisionless (zero) sound. There are significant efforts underway to study transport processes such as mass and spin edge currents^{12,13,48}, thermal Hall effects¹⁴, thermal conductivity¹⁹ and spin diffusion in highly confined geometries, where the suppression of T_c and strong confinement should lead to the enhancement of the contribution of fluctuations,

potentially impacting exotic topological transport.

Methods

Quartz fork: The experimental results described here were obtained with a quartz fork³⁴ with dimensions much greater than the quasiparticle mean free path. The other relevant length scale is the viscous penetration depth, $\delta = (2\eta/\rho\omega)^{1/2}$, where η and ρ are the viscosity and density of the ³He, while ω is the resonant frequency of the fork. The largest value of the viscous penetration depth occurs at T_c at 0 bar. Unlike collisionless sound where $\omega\tau \geq 1$, here the fork operates in the hydrodynamic limit ($\omega\tau \leq 1$) with $\omega = 2\pi f_0 \approx 2 \times 10^5 \text{ s}^{-1}$ and $\tau \approx 2 \times 10^{-6} \text{ s}$ at $p = 0$ bar and $T = T_c$ (see Supplementary Note 1 for further details).

Fork operation: The quartz fork was operated in a phase locked loop and driven at a fixed drive voltage. The phase locked loop was set to drive the fork at a frequency fixed to within 5 Hz from resonance. When the frequency shift exceeded these bounds, the drive frequency was adjusted to bring the device on resonance again. The resonant frequency and Q were inferred from the complex response recorded by the lock in amplifier. In order to simplify this conversion, a significant background response of the non-resonant signal (“feedthrough”) had to be measured and subtracted from the received signal. After subtraction, when the drive frequency was swept through resonance, the signal was seen to be Lorentzian, and was calibrated to yield the Q . Further details are provided in the Supplementary Note 2.

Thermometry: Thermometry was accomplished using a small pill (1.25 mm diameter, 1.25 mm

high) of $\leq 30 \mu\text{m}$ diameter powdered Lanthanum diluted Cerous Magnesium Nitrate (LCMN), packed to 50% density. The pill and monitoring coil were located in a niobium shielding can. The coil structure consisted of an astatically wound secondary and primary coil. The primary coil was driven at constant voltage through a $10 \text{ k}\Omega$ resistor by a signal generator at fixed frequency (23Hz). The secondary coil was coupled to the input of a SQUID. The secondary loop had an additional mutual inductor to allow cancellation of the induced signal in the loop. The input of this mutual inductor was driven by the same signal generator as the primary. The drive amplitude and phase of this cancellation signal was stepped by discrete amounts to cancel out most of the current in the secondary loop. The drive applied to the mutual inductor and the magnitude of the received signal were proportional to the susceptibility of the LCMN. These were calibrated against a melting curve thermometer and against the superfluid transition temperatures at various pressures. The thermometer had a resolution of better than 50 nK .

1. Emery, V. Fluctuations above the superfluid transition in liquid ^3He . *Journal of Low Temperature Physics* **22**, 467 (1978). URL <https://doi.org/10.1007/BF00654719>.
2. Anderson, P. W. Localized magnetic states in metals. *Phys. Rev.* **124**, 41–53 (1961). URL <https://link.aps.org/doi/10.1103/PhysRev.124.41>.
3. Aslamazov, L. G. & Larkin, A. I. Effect of fluctuations on the properties of a superconductor above the critical temperature. In *30 Years of the Landau Institute — Selected Papers*, 23–28 (WORLD SCIENTIFIC, 1996).
4. Randeria, M. & Taylor, E. Crossover from Bardeen – Cooper – Schrieffer

- to Bose – Einstein Condensation and the Unitary Fermi gas. *Annual Review of Condensed Matter Physics* **5**, 209–232 (2014). URL <https://doi.org/10.1146/annurev-conmatphys-031113-133829>.
5. Mueller, E. J. Review of pseudogaps in strongly interacting Fermi gases. *Reports on Progress in Physics* **80**, 104401 (2017). URL <https://doi.org/10.1088/1361-6633/aa7e53>.
 6. Timusk, T. & Statt, B. The pseudogap in high-temperature superconductors: an experimental survey. *Reports on Progress in Physics* **62**, 61–122 (1999). URL <https://doi.org/10.1088/0034-4885/62/1/002>.
 7. Lipa, J. A., Swanson, D. R., Nissen, J. A., Chui, T. C. P. & Israelsson, U. E. Heat capacity and thermal relaxation of bulk helium very near the lambda point. *Phys. Rev. Lett.* **76**, 944–947 (1996). URL <https://link.aps.org/doi/10.1103/PhysRevLett.76.944>.
 8. Mizushima, T., Tsutsumi, Y., Sato, M. & Machida, K. Symmetry protected topological superfluid ^3He – B. *Journal of Physics: Condensed Matter* **27**, 113203 (2015). URL <https://dx.doi.org/10.1088/0953-8984/27/11/113203>.
 9. Abrikosov, A. A. & Khalatnikov, I. M. The theory of a fermi liquid (the properties of liquid ^3He at low temperatures). *Reports on Progress in Physics* **22**, 329–367 (1959). URL <https://doi.org/10.1088/0034-4885/22/1/310>.
 10. Ginzburg, V. & Landau, L. Phenomenological theory. *J. Exp. Theor. Phys. USSR* **20**, 17 (1950).

11. Larkin, A. I. & Varlamov, A. A. *Fluctuation Phenomena in Superconductors* (Springer, Berlin, Heidelberg, 2008).
12. Sauls, J. A. Surface states, edge currents, and the angular momentum of chiral p -wave superfluids. *Phys. Rev. B* **84**, 214509 (2011). URL <https://link.aps.org/doi/10.1103/PhysRevB.84.214509>.
13. Wu, H. & Sauls, J. A. Majorana excitations, spin and mass currents on the surface of topological superfluid ^3He – B. *Phys. Rev. B* **88**, 184506 (2013). URL <https://link.aps.org/doi/10.1103/PhysRevB.88.184506>.
14. Sharma, P., Vorontsov, A. B. & Sauls, J. A. Disorder induced anomalous thermal hall effect in chiral phases of superfluid ^3He (2022). URL <https://arxiv.org/abs/2209.04004>.
15. Levitin, L. V. *et al.* Phase Diagram of the Topological Superfluid ^3He Confined in a Nanoscale Slab Geometry. *Science* **340**, 841–844 (2013). URL <http://science.sciencemag.org/content/340/6134/841>.
16. Levitin, L. *et al.* Surface-Induced Order Parameter Distortion in Superfluid ^3He -B Measured by Nonlinear NMR. *Physical Review Letters* **111**, 235304 (2013). URL <http://dx.doi.org/10.1103/PhysRevLett.111.235304>.
17. Zhelev, N. *et al.* The A-B transition in superfluid helium-3 under confinement in a thin slab geometry. *Nature Communications* **8**, 15963 (2017). URL <http://dx.doi.org/10.1038/ncomms15963>.

18. Heikkinen, P. J. *et al.* Fragility of surface states in topological superfluid ^3He . *Nature Communications* **12**, 1574 (2021). URL <https://doi.org/10.1038/s41467-021-21831-y>.
19. Lotnyk, D. *et al.* Thermal transport of helium-3 in a strongly confining channel. *Nature Communications* **11**, 4843 (2020). URL <https://doi.org/10.1038/s41467-020-18662-8>.
20. Lotnyk, D. *et al.* Path-dependent supercooling of the ^3He superfluid A – B transition. *Phys. Rev. Lett.* **126**, 215301 (2021). URL <https://link.aps.org/doi/10.1103/PhysRevLett.126.215301>.
21. Paulson, D. N. & Wheatley, J. C. Incipient superfluidity in liquid ^3He above the superfluid transition temperature. *Phys. Rev. Lett.* **41**, 561–564 (1978). URL <https://link.aps.org/doi/10.1103/PhysRevLett.41.561>.
22. Samalam, V. K. & Serene, J. W. Zero-sound attenuation from order-parameter fluctuations in liquid ^3He . *Phys. Rev. Lett.* **41**, 497–500 (1978). URL <https://link.aps.org/doi/10.1103/PhysRevLett.41.497>.
23. McClintock, P. V. E. Incipient superfluidity in normal liquid ^3He . *Nature* **275**, 585–586 (1978). URL <https://doi.org/10.1038/275585a0>.
24. Lee, Y. *et al.* High frequency acoustic measurements in liquid ^3He near the transition temperature. *Journal of Low Temperature Physics* **103**, 265–272 (1996). URL <https://doi.org/10.1007/BF00754788>.

25. Granroth, G. E., Masuhara, N., Ihas, G. G. & Meisel, M. W. Broadband frequency study of the zero sound attenuation near the quantum limit in normal liquid ^3He close to the superfluid transition. *Journal of Low Temperature Physics* **113**, 543–548 (1998). URL <https://doi.org/10.1023/A:1022576817674>.
26. Pal, A. & Bhattacharyya, P. Fluctuation contribution to the velocity and damping of sound in liquid ^3He above the superfluid transition temperature. *Journal of Low Temperature Physics* **37**, 379–387 (1979). URL <https://doi.org/10.1007/BF00119195>.
27. Lin, W.-T. & Sauls, J. A. Effects of incipient pairing on nonequilibrium quasiparticle transport in Fermi liquids. *Progress of Theoretical and Experimental Physics* **2022** (2022). URL <https://doi.org/10.1093/ptep/ptac027>.
28. Parpia, J. M., Sandiford, D. J., Berthold, J. E. & Reppy, J. D. Viscosity of liquid $^3\text{He} - \text{B}$ near the superfluid transition. *Phys. Rev. Lett.* **40**, 565–568 (1978). URL <https://link.aps.org/doi/10.1103/PhysRevLett.40.565>.
29. Tian, Y., Smith, E., Reppy, J. & Parpia, J. Anomalous inferred viscosity and normal density in a torsion pendulum. *Journal of Low Temperature Physics* **205**, 226–234 (2021). URL <https://doi.org/10.1007/s10909-021-02619-2>.
30. Carless, D. C., Hall, H. E. & Hook, J. R. Vibrating wire measurements in liquid ^3He . I. The normal state. *Journal of Low Temperature Physics* **50**, 583–603 (1983). URL <https://doi.org/10.1007/BF00683497>.
31. Nakagawa, M., Matsubara, A., Ishikawa, O., Hata, T. & Kodama, T. Viscosity mea-

- surements in normal and superfluid ^3He . *Phys. Rev. B* **54**, R6849–R6852 (1996). URL <https://link.aps.org/doi/10.1103/PhysRevB.54.R6849>.
32. Greywall, D. ^3He specific heat and thermometry at millikelvin temperatures. *Physical Review B* **33**, 7520 – 7538 (1986). URL <http://dx.doi.org/10.1103/PhysRevB.33.7520>.
33. Greywall, D. Thermal conductivity of normal liquid ^3He . *Physical Review B* **29**, 4933 – 4945 (1984). URL <http://dx.doi.org/10.1103/PhysRevB.29.4933>.
34. Blaauwgeers, R. *et al.* Quartz tuning fork: Thermometer, pressure- and viscometer for helium liquids. *Journal of Low Temperature Physics* **146**, 537–562 (2007). URL <https://doi.org/10.1007/s10909-006-9279-4>.
35. Morley, G. W. *et al.* Torsion pendulum for the study of thin ^3He films. *Journal of Low Temperature Physics* **126**, 557–562 (2002). URL <https://doi.org/10.1023/A:1013767117903>.
36. Rusby, R. *et al.* Realization of the ^3He Melting Pressure Scale, PLTS-2000. *J. Low Temp. Phys.* **149**, 156–175 (2007).
37. Tian, Y., Smith, E. & Parpia, J. Conversion between ^3He melting curve scales below 100 mk. *Journal of Low Temperature Physics* **208**, 298–311 (2022). URL <https://doi.org/10.1007/s10909-022-02721-z>.
38. Parpia, J. M. & Rhodes, T. L. First observation of the Knudsen mini-

- mum in normal liquid ^3He . *Phys. Rev. Lett.* **51**, 805–808 (1983). URL <https://link.aps.org/doi/10.1103/PhysRevLett.51.805>.
39. Parpia, J. *et al.* Optimization procedure for the cooling of liquid ^3He by adiabatic demagnetization of praseodymium nickel. *Review of Scientific Instruments* **56**, 437 – 443 (1985). URL <http://dx.doi.org/10.1063/1.1138319>.
40. Alvesalo, T. A., Anufriyev, Y. D., Collan, H. K., Lounasmaa, O. V. & Wennerström, P. Evidence for superfluidity in the newly found phases of ^3He . *Phys. Rev. Lett.* **30**, 962–965 (1973). URL <https://link.aps.org/doi/10.1103/PhysRevLett.30.962>.
41. Pethick, C. J., Smith, H. & Bhattacharyya, P. Viscosity and thermal conductivity of superfluid ^3He : Low-temperature limit. *Phys. Rev. Lett.* **34**, 643–646 (1975). URL <https://link.aps.org/doi/10.1103/PhysRevLett.34.643>.
42. Bhattacharyya, P., Pethick, C. J. & Smith, H. Transport and relaxation processes in superfluid ^3He close to the transition temperature. *Phys. Rev. B* **15**, 3367–3383 (1977). URL <https://link.aps.org/doi/10.1103/PhysRevB.15.3367>.
43. Parpia, J. *The Viscosity of Normal and Superfluid ^3He* . Ph.D. thesis, Cornell University (1979).
44. Greywall, D. S. Specific heat of normal liquid ^3He . *Phys. Rev. B* **27**, 2747–2766 (1983). URL <https://link.aps.org/doi/10.1103/PhysRevB.27.2747>.
45. Roach, P. R. & Ketterson, J. B. Observation of transverse zero sound in normal ^3He . *Phys. Rev. Lett.* **36**, 736–740 (1976). URL <https://link.aps.org/doi/10.1103/PhysRevLett.36.736>.

46. Sharma, P. Anomalous Heat and Momentum Transport Arising from Surface Roughness in a Normal ^3He Slab. *Journal of Experimental and Theoretical Physics* **126**, 201–209 (2018). URL <https://doi.org/10.1134/S1063776118020073>.
47. Autti, S. *et al.* Fundamental dissipation due to bound fermions in the zero-temperature limit. *Nature Communications* **11**, 4742 (2020). URL <https://doi.org/10.1038/s41467-020-18499-1>.
48. Wu, H. & Sauls, J. A. Majorana excitations, spin and mass currents on the surface of topological superfluid $^3\text{He} - \text{B}$. *Phys. Rev. B* **88**, 184506 (2013). URL <https://link.aps.org/doi/10.1103/PhysRevB.88.184506>.

Acknowledgements This work was supported by the National Science Foundation, under DMR-2002692 (JMP), and PHY-2110250 (EJM).

Author contributions statement Experimental work was principally carried out by Y.T. and R.B. with further support from E.N.S. and J.M.P. Analysis and the presentation of figures was carried out by R.B. and Y.T.. We thank Anna Eyal for generating the figure of the cell in Figure 1. E.M significantly contributed to the analysis and the writing of the manuscript, J.M.P. supervised the work and J.M.P., and E.M. had leading roles in formulating the research and writing this paper. R.B and Y.T contributed equally to the publication of this result. All authors contributed to revisions to the paper.

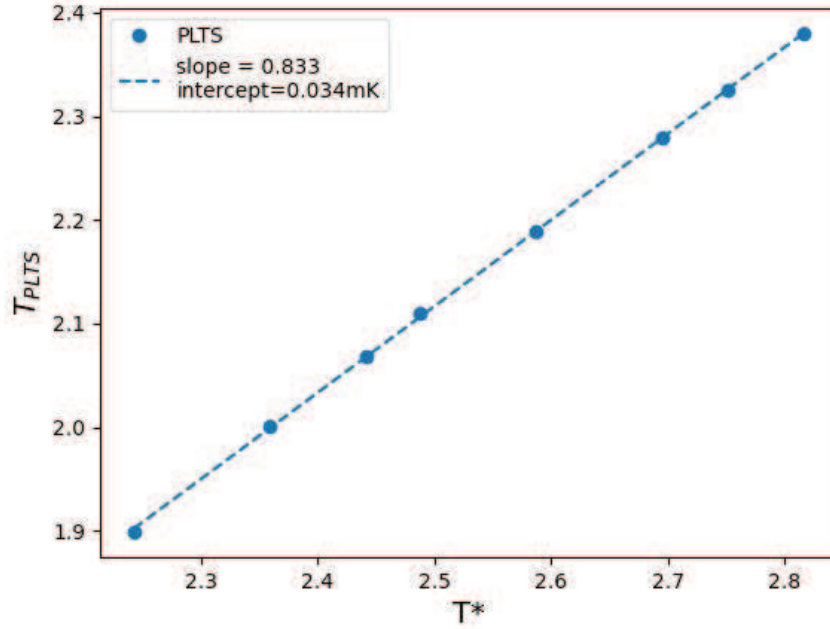
Correspondence All correspondence should be directed to jmp9@cornell.edu

Data Availability The data generated in this study and shown in all the plots in this paper and the supplementary material have been deposited in the Cornell University e-commons data repository database under accession code <https://doi.org/10.7298/r4jy-py94>.

Additional information

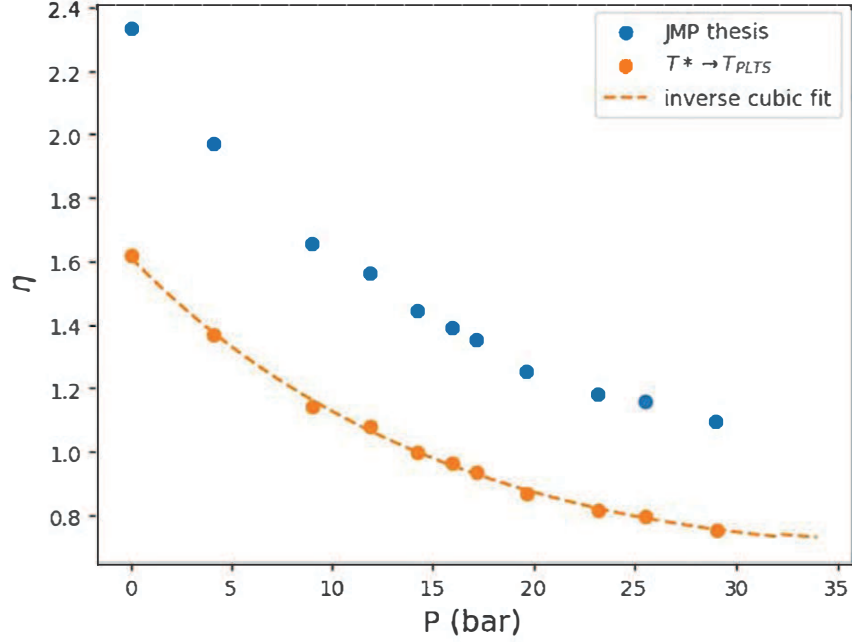
Competing Interests: The authors declare that they have no competing interests.

Supplementary Note 1: Calculation of $\tau_\eta T^2$ and other parameters



Supplementary Figure 1: **Conversion from T^* to T_{PLTS} .** Values of T_c^* [1,2] plotted against values of T_c on the *PLTS* scale^{S3,S4}.

To arrive at an estimate for the magnitude of the fluctuation contribution to the Q , we need to determine various pressure dependent quantities for liquid ^3He . We start with the determination of $\tau_\eta T^2$, the quasiparticle scattering time associated with the viscosity. The Fermi liquid viscosity was studied by Parpia and co-workers^{S1,S2}. The temperature scale used in that work needs to be converted to the PLTS scale^{S3}. We plot the values of T_c^* against the values of T_c in the PLTS scale^{S4} in Supplementary Figure 1. The conversion requires a linear scaling with a small offset, yielding $T_{PLTS} = 0.833T^* + 0.034$. The pressure dependent viscosity coefficients ηT^2 [poise-mK²] listed in Ref[1] are then converted to their values with the PLTS scale.



Supplementary Figure 2: ηT^2 vs **Pressure**. Values of the viscosity coefficient^{S1} before conversion (blue) and after conversion to the PLTS scale (gold). The dashed line is a cubic fit to $\eta(P)T^2$.

The viscosity coefficient, $\eta(P)T^2$ (η in poise, P in bar, T in mK following the PLTS scale), shown in Supplementary Figure 2 and listed in Supplementary Table 1, can be calculated from the relation,

$$(\eta(P)T^2)^{-1} = \sum_{i=0}^3 A_i P^i,$$

with

$$A_0 = 6.18470415 \times 10^{-1}, \quad A_1 = 2.49235869 \times 10^{-2},$$

$$A_2 = 2.33758602 \times 10^{-4}, \quad A_3 = -9.37151796 \times 10^{-6}.$$

(5)

The viscosity of ^3He can be written as

$$\eta = \frac{1}{5} n p_F \lambda = \frac{1}{5} n m \left(\frac{m^*}{m} \right) v_F^2 \tau,$$

thus (6)

$$\tau(P) T^2 = 5 \eta(P) T^2 \frac{V_m}{5.009 \times 10^{-24} \times N_A} \frac{1}{(m^*/m) v_F^2},$$

with p_F and v_F the Fermi momentum and velocity respectively, n , the particle density, λ the quasiparticle mean free path, τ the viscous scattering time, V_m the molar volume, N_A , Avogadro's number, and m^*/m the effective mass ratio. The mass of each ^3He atom, $m = 5.009 \times 10^{-24}$ g, is also needed to obtain the mass density.

The molar volume (in cm^3 , with P in bar) is reproduced from Reference [5].

$$V_m = \sum_{i=0}^5 B_i P^i,$$

with

$$B_0 = 36.837231, \quad B_1 = -1.1803474, \quad (7)$$

$$B_2 = 8.3421417 \times 10^{-2}, \quad B_3 = -3.8859562 \times 10^{-3},$$

$$B_4 = 9.475978 \times 10^{-5}, \quad B_5 = -9.1253577 \times 10^{-7}.$$

The effective mass was obtained by fitting a polynomial to the data in Reference [5].

$$\frac{m^*}{m} = \sum_{i=0}^4 C_i P^i,$$

with

$$\begin{aligned} C_0 &= 2.80, & C_1 &= 0.1292, \\ C_2 &= -3.188 \times 10^{-3}, & C_3 &= 9.372 \times 10^{-5}, \\ C_4 &= -1.03 \times 10^{-6}. \end{aligned} \tag{8}$$

The Fermi velocity was obtained by fitting a polynomial to the data in Reference [5]

$$v_F = \sum_{i=0}^4 D_i P^i,$$

with

$$\begin{aligned} D_0 &= 59.8353052512899, & D_1 &= -1.99579000023344, \\ D_2 &= 8.19564928730876 \times 10^{-2}, & D_3 &= -2.10299440496278 \times 10^{-3}, \\ D_4 &= 2.13615981987922 \times 10^{-5}. \end{aligned} \tag{9}$$

A polynomial fit to $T_c(P)$ on the PLTS scale is provided in Reference [4] and listed here

$$T_{c,PLTS} = \sum_{i=0}^5 E_i P^i,$$

with

$$E_0 = 0.90972399274531, \quad E_1 = 0.14037182852625, \quad (10)$$

$$E_2 = -0.0074017331747577, \quad E_3 = 2.8617547367067 \times 10^{-4},$$

$$E_4 = -6.5064429600510 \times 10^{-6}, \quad E_5 = 6.0754459040296 \times 10^{-8}.$$

We use Supplementary Equations 5, 6, 7, 8, 9 to calculate $\tau_\eta T^2$ and then Supplementary Equation 6, 10 to calculate the quasiparticle scattering time at T_c , τ_c . We also need T_F to calculate the quantity $C(P)$ in Equation 4 of the main paper. We use Equation 6 in Reference [6] together with Supplemental Equation 8 to calculate T_F (K), using V_m in cc/mole.

$$T_F = \frac{\hbar^3}{2mk_B(m^*/m)} \left(\frac{3\pi^2}{V_m} \right)^{2/3} = \frac{54.91}{m^*/m} V_m^{-2/3}. \quad (11)$$

Values for the coefficient $\tau_\eta T^2$, τ_c , T_c , V_m , v_F , T_F and m^*/m at various pressures are listed in Supplementary Table 1. These values can be used along with the best fit determination of $\alpha = 0.434$ and $\Gamma = 40.8$ to obtain values for $C(P)$ in Equation 3 of the main paper, which also relates to $\delta Q_c/Q_c$, the maximum contribution to the excess Q at the transition temperature plotted in Figure 3 a) of the main paper.

The hydrodynamic regime ($\omega\tau \leq 1$), is distinct from the collisionless regime ($\omega\tau \geq 1$).

In the hydrodynamic regime, collisions are frequent compared to the frequency of the external excitation (*e.g.* pressure oscillation or shear frequency). In the collisionless regime, the excitation frequency exceeds the inverse mean time between collisions. In our experiment, the largest value of $\omega\tau_c$ is attained for $P = 0$ and T_c and is calculated to be ≈ 0.243 (see Supplementary Table 1). In the first observation of collisionless sound^{S7}, the attenuation of first sound is $\approx 4\%$ below the expected normal state value for $\omega\tau \approx 0.25$. Thus, it is possible that at the lowest pressure, a portion of the deviation from $Q \propto T$ is due to a deviation from hydrodynamic behavior. However, such a contribution would be distributed over a range of temperature and not confined to the region near T_c . Additionally, the increase in T_c with pressure and the decrease of the coefficient ηT^2 (and τT^2) with pressure assures us that the departure from Fermi-liquid behavior cannot be accounted for by non-equilibrium effects due to any departure from the ideal $\omega\tau \ll 1$ regime.

The mean free path (λ_η) should be smaller than the viscous penetration depth $\delta=(2\eta/\rho\omega)$, which is the distance over which the transverse velocity field in a fluid of density ρ , viscosity η , in contact with an object oscillating at a frequency ω , decays exponentially. The mean free path should also be smaller than the confinement size. These conditions are met well at high pressure, and marginally at low pressure (see Supplementary Table 1). Once again, the observation of the departure from Fermi-liquid behavior is strongest at high pressure, where the conditions for hydrodynamic behavior are well fulfilled.

Pressure [bar]	0	3	6	9	12	15	18	21	24	27	30
$\tau_\eta T^2 [\mu smK^2]$	0.985	0.861	0.776	0.712	0.660	0.616	0.597	0.550	0.529	0.515	0.508
$\tau_c [\mu s]$	1.19	0.533	0.328	0.234	0.182	0.149	0.127	0.111	0.100	0.0933	0.0887
$T_c [mK]$	0.9097	1.271	1.539	1.743	1.903	2.033	2.139	2.226	2.296	2.351	2.392
$T_F [K]$	1.77	1.66	1.56	1.49	1.42	1.36	1.31	1.26	1.22	1.17	1.13
$V_m [cm^3]$	36.84	33.95	32.03	30.71	29.71	28.89	28.18	27.55	27.01	26.56	26.17
m^*/m	2.80	3.16	3.48	3.77	4.03	4.28	4.53	4.77	5.02	5.26	5.50
$v_F [m/s]$	59.83	54.53	50.38	47.11	44.49	42.32	40.44	38.74	37.15	35.65	34.24
$\delta Q/Q_c$	0.0176	0.0244	0.0302	0.0343	0.0382	0.0416	0.0445	0.0474	0.0500	0.0544	0.0582
$\omega\tau_c$	0.243	0.109	0.0670	0.0478	0.0372	0.0304	0.0259	0.0227	0.0204	0.0191	0.0181
$\lambda_\eta(T_c) [\mu m]$	71.2	29.1	16.5	11.0	8.10	6.31	5.14	4.30	3.72	3.33	3.04
$\lambda_\eta(3 mK) [\mu m]$	6.55	5.22	4.35	3.72	3.26	2.90	2.61	2.37	2.18	2.04	1.93
$\eta(T_c) [\text{poise}]$	1.97	0.890	0.544	0.384	0.296	0.239	0.202	0.174	0.155	0.141	0.132
$\delta_c [\mu m]$	154	99.2	75.3	61.9	53.5	47.4	43.0	39.6	36.9	35.0	33.5

Table 1: **Supplementary Table 1: Fermi liquid parameters**

Lists various quantities to estimate the fluctuation contribution in Equation 3, Main article, and for the discussion concerning mean free paths.

Supplementary Note 2: Background correction procedure

Outline of procedure

In this Supplementary Note, we describe details of the procedure we followed to correctly subtract the non-resonant background signal from our quartz tuning fork. The quartz fork is driven and detected through its in-built piezo electric capability. The distinguishing feature of our data on Q is the fact that we are able to track the quartz fork's Q continuously at all pressures. This is enabled by our use of a digital phase locked loop (PLL) that keeps the quartz fork on or near resonance. There is significant electrical coupling of the drive signal to the output side, with an attendant frequency dependent phase shift. The loop requires that the received vector signal $X(T), Y(T)$ from the lock in amplifier, has the non-resonant signal (feed through) subtracted from the received signal (See Supplementary Figure 3). When operated in vacuum, the fork's Q is high enough so that the received signal displays a Lorentzian response without background subtraction. When operated in liquid ^3He at low temperatures, the fork's Q can be as low as ≈ 10 leading to a broad response with a correspondingly small resonant signal requiring subtraction of the background signal for further analysis.

The subtraction procedure was carried out while gathering the data within the LabView Virtual Instrument environment. However, after the data was accumulated at several pressures, it became apparent that the original background calibration was insufficiently precise and that a post processing procedure would have to be followed. If the fitted background was used "as is", the result would be a non-Lorentzian resonance seen in the red trace in Supplementary Figure 5. (The

background subtraction and effects are shown in Supplementary Figures 3, 4, 5). An important condition imposed was that the Q vs T plot have a $Q(T = 0) = 0$ conforming with Fermi liquid behavior expectations. During our temperature sweep we adjusted the drive frequency when it differed from the inferred resonant frequency by 5 Hz. If the background subtraction is not performed correctly one finds small jumps in the inferred Q and resonant frequency. We used the elimination of these jumps as an additional constraint.

This Supplementary note details the procedure for all post-acquisition adjustments at one pressure (29.3 bar). Briefly, the procedure consisted of

1. A linear fit to the “as collected” Q vs T for temperatures between $1.2T_c$ and $1.4T_c$ yielded the intercept, $Q(0)_1$, listed as the first iteration of the correction procedure in Supplementary Table 2. $Q(0)_1$ was converted to signal units (Volts) using a constant k (defined later), and was subtracted from the $X(T)$ data, shown in Supplementary Figure 6. This “enforced” expectations of Fermi liquid behavior in the normal liquid ($\eta \rightarrow \infty$ as $T \rightarrow 0$).
2. The Nyquist trace $Y(T)$ vs $X(T)$ was plotted for each constant pressure cooldown. Circular arcs of constant Q were drawn for each drive-frequency reset, shown in Supplementary Figure 7a). The $X(T)$ data segments for a given fixed drive frequency were shifted to the nearest constant Q arc, shown in Supplementary Figure 7b). This was done to eliminate the slightly jagged character of the Q vs T plot. The mean displacement between $X(T)$ and its nearest constant Q arc (denoted as $\overline{\Delta Q_1}$) is the mean jump in Q found in the “as collected” data and is tabulated in Supplementary Table 2. $Q(T)$ was recalculated with the corrected

$X(T)$ data and the “as collected” $Y(T)$ data. This completes the first iteration of X offset corrections.

3. A linear fit to the recalculated $Q(T)$ data between $1.2T_c$ and $2T_c$ (or the highest temperature in the run), yielded $Q(0)_2$, the intercept in the second iteration of the X offset correction procedure (tabulated in Supplementary Table 2). $Q(0)_2$ was converted to Volts with the k constant, and was subtracted from the $X(T)$ data. The Nyquist trace was plotted, and circular arcs of constant Q were calculated for each frequency reset point. $X(T)$ data segments at fixed drive frequency were shifted onto the nearest constant Q arc. The mean displacement between $X(T)$ and its nearest constant Q arc, $\overline{\Delta Q_2}$, the mean jump in Q found in the second iteration of X offset corrections, is tabulated in Supplementary Table 2. The $Q(T)$ is recalculated with the corrected $X(T)$ data and the “as collected” $Y(T)$ data. This completes the second iteration of X offset corrections.

4. A linear fit to the doubly recalculated $Q(T)$ data for temperatures between $1.2T_c$ and $2T_c$ (or the highest temperature in the run), yields $Q(0)_3$, the intercept in the second iteration of the X offset correction procedure tabulated in Supplementary Table 2. $Q(0)_3$ was converted to Volts with the k constant, and was subtracted from the $X(T)$ data. The Nyquist trace was plotted, and the circular constant Q arcs were calculated and drawn at each frequency reset point. $X(T)$ data segments for a fixed drive frequency were shifted onto the nearest constant Q arc. The mean displacement between $X(T)$ and its nearest constant Q arc, $\overline{\Delta Q_3}$, (the mean jump in Q found in the third iteration of X offset corrections) is tabulated in Supplementary Table 2. The $Q(T)$ was recalculated with the corrected $X(T)$ data and the

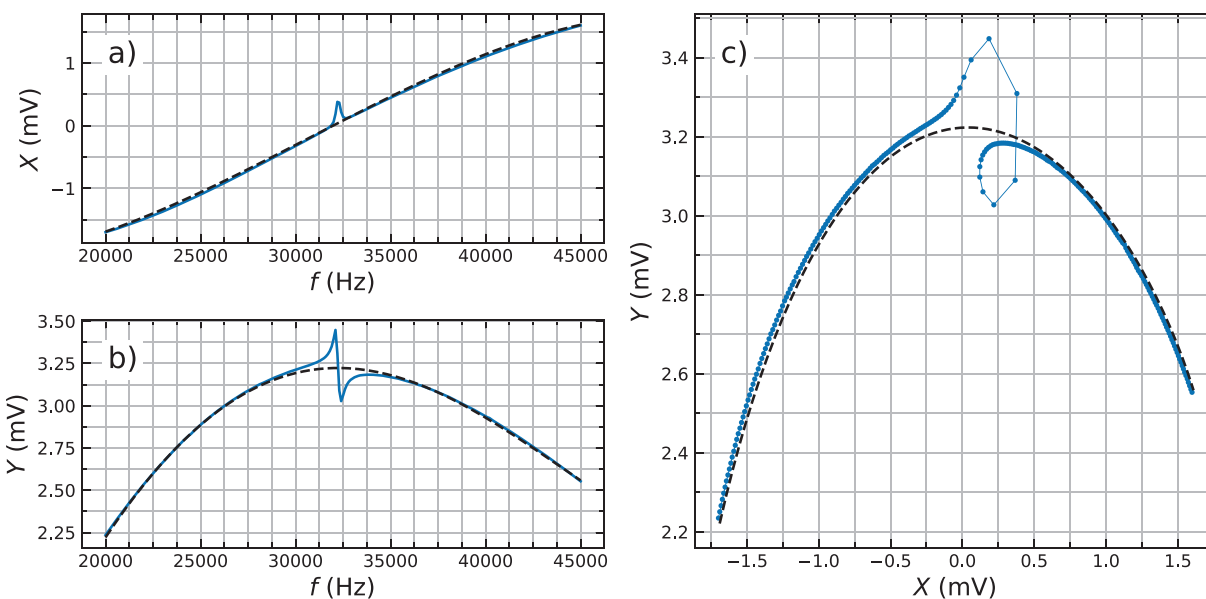
“as collected” $Y(T)$ data. This completes the third iteration of X offset corrections.

5. The resonant frequency, $f_o(T)$, was recalculated after the three iterations of X offset corrections. It displayed discontinuous line segments, with jumps in $f_o(T)$ at each frequency reset point. (See Supplementary Figure 8). The sum of the jumps at each f_o was minimized by multiplying the “originally set” k in LabView by a multiplicative constant, k_{adj} , listed Supplementary Table 2. The final $Q(T)$ was recalculated with the new scaling constant $k_{adj} \times k$. A linear fit to the $Q(T)$ for temperatures between $1.2T_c$ and $2T_c$ (or the highest temperature in the run) was obtained, and its slope T_c is the Q_c reported in the main body of the paper. The intercept of this line is the final intercept quoted in Supplementary Table 2. Supplementary Figure 9 compares the final recalculation of $Q(T)$ and its linear fit, with the “as collected” $Q(T)$ and the linear fit calculated in step 1.

In the following, we provide more details accompanied by figures to clarify the procedure. Importantly, the fluctuation precursor is seen in the “raw data” before the various iterations at all pressures. The post data-acquisition procedure is needed to provide the “Fermi liquid background” behavior to scale the fluctuation contribution. We list the procedure and details so that other users may adapt it for their own investigations. Elimination or significant reduction of the non-resonant background signal is essential to resolve any finer detailed variation of the fluctuation contribution. Ultimately, the ability to continuously track the Q together with the high resolution thermometry enabled the fluctuation contribution to the viscosity of ^3He to be resolved in this experiment.

Background subtraction and first iteration.

As stated in the summary, we recorded values of $X(T), Y(T)$ obtained while driving a quartz resonator at a frequency, f_D near the fork's resonant frequency, f_0 immersed in ^3He . To calculate the Q and f_0 , the non-resonant signal has to be first subtracted from the received signal.



Supplementary Figure 3: **Quartz tuning fork background sweep.** The response of a quartz tuning fork at 8.1 mK and 29.3 bar over a wide frequency range. The dashed lines are the fitted 3rd order and 4th order polynomials for the X a) and Y b) responses after the correction noted to fit a Lorentzian to the fork's resonance (see Supplemental Figure 4). In panel c) we compare the fit (dashed line) to the observed complex response.

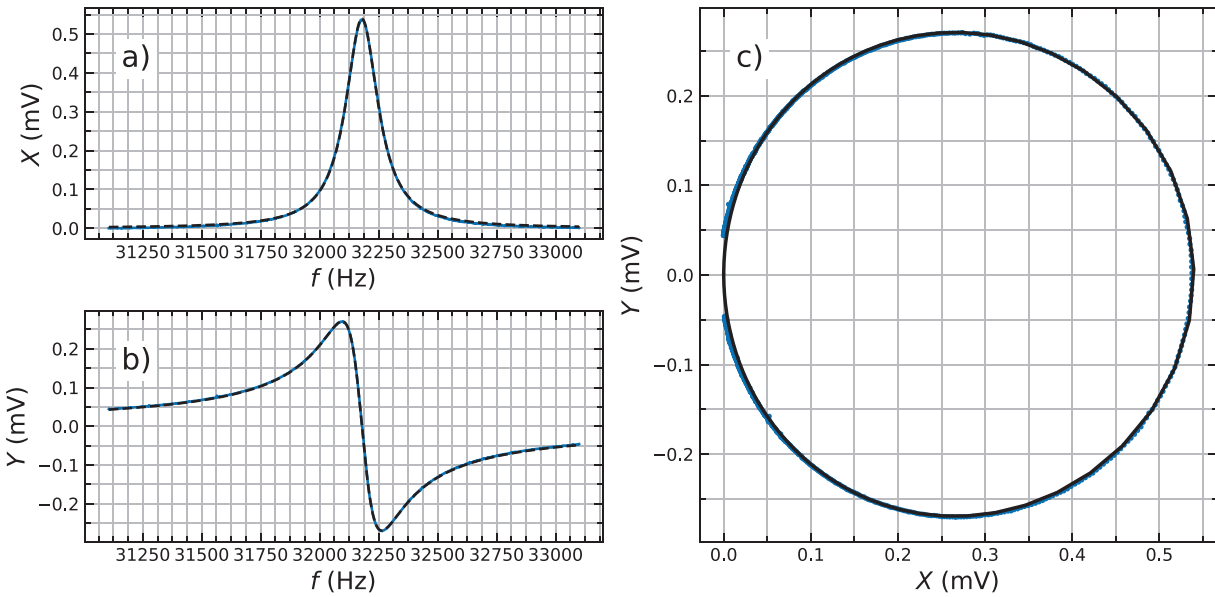
To effect this subtraction, we first carried out a sweep from 20 kHz through 45 kHz at ≈ 100 mK (not shown here) where the resonant line is narrow. This was done to assess the background

and allow the fork to be operated while cooling down to dilution refrigerator temperatures. At lower temperatures (8.1 mK shown in Supplementary Figure 3), we repeated this sweep. We then swept the frequency through the resonance over a frequency range spanning a few linewidths. We found that the X channel could be fit to a 3rd order polynomial, and the Y channel required a 4th order polynomial to adequately fit the background. After subtraction of these backgrounds, we plot the narrow range signal and obtain a Lorentzian fit for the resonance. A Nyquist plot with the real axis aligned along the X channel and the out-of-phase response aligned along Y reveal a near perfect circle plot. These X and Y signals (after subtraction of the fitted background), together with the associated Nyquist plot are shown in Supplementary Figure 4. In order to obtain a satisfactory Lorentzian fit a small ($\leq +0.05$ mV) shift to the fitted background was needed. This increase in X accounts for the difference between the fit used (shown as a dashed line) and the data shown in Supplementary Figure 3. The Lorentzian is used to obtain the $Q = Q_R$, and the amplitude of the signal at resonance (A_R) is also noted. The previously mentioned constant k is defined as $k = Q_R/A_R$. (The value of k used in the LabView VI was likely not accurate enough and necessitated adjustments described in the following sections). Together with the $X(T)$ and $Y(T)$ (X, Y values after subtraction of the background at any temperature T), these constitute the inputs to the determination of the resonant frequency $f(T)$ and the $Q(T)$ using the equations^{S8},

$$Q(T) = \frac{X(T)^2 + Y(T)^2}{X(T)} \left(\frac{Q_R}{A_R} \right) \quad (12)$$

$$f(T) = f_D(T) \left(1 + \frac{Y(T)}{X(T)} \frac{1}{2Q_T} \right) \quad (13)$$

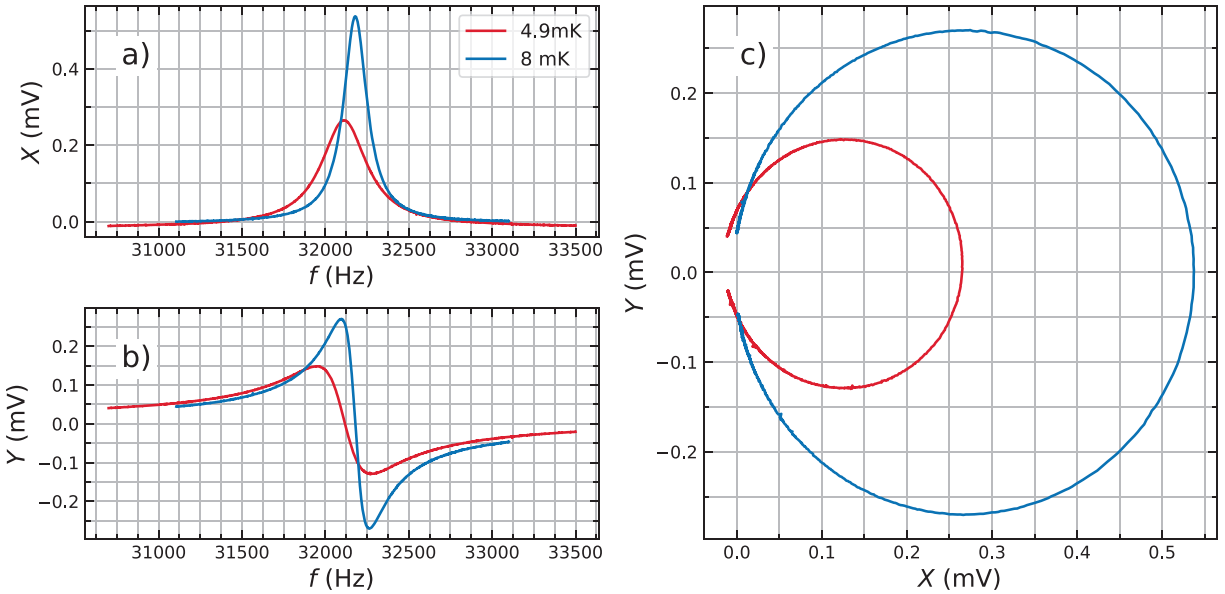
where $f_D(T)$ is the drive frequency at any temperature, T . These equations form the basis of the PLL that maintains the fork within ± 5 Hz of resonance and were used to calculate the “raw” values of $Q(T)$ and $f(T)$.



Supplementary Figure 4: **Quartz tuning fork Lorentzian response.** The response of a quartz tuning fork at 8.1 mK and 29.3 bar after subtraction of the background. The black (dashed/solid) lines on the (left/right) are the fitted curves to a Lorentzian response.

When we apply the same background subtraction to a frequency sweep at 4.9 mK (obtained a few days later), where the Q is further reduced, the Nyquist response within the linewidth is horizontally off-center. This offset in the X background is not systematically temperature dependent.

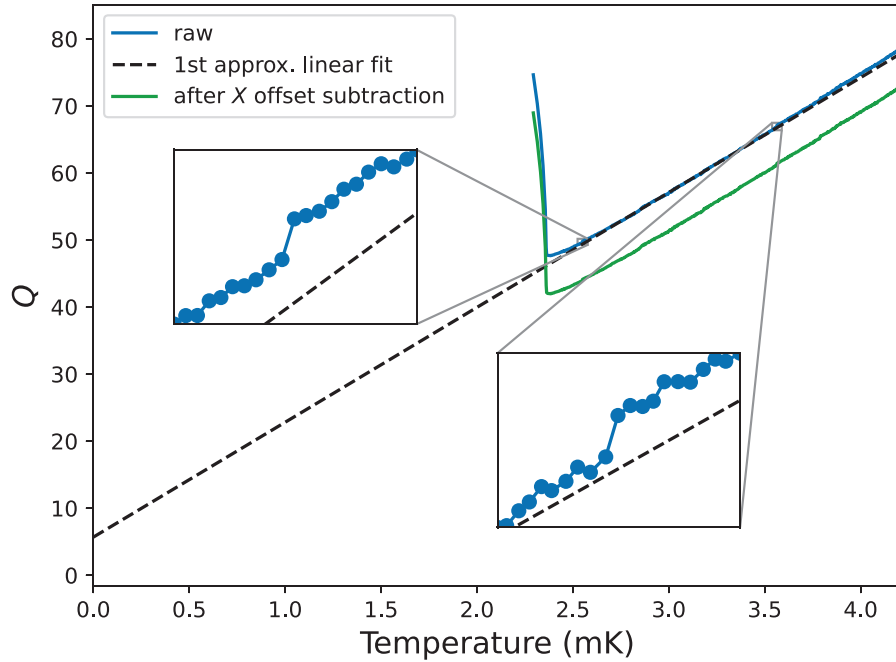
Instead it appears that there is a small frequency dependence to the background (corresponding to a first order term) that is not captured in our background subtraction procedure.



Supplementary Figure 5: **Quartz tuning fork Lorentzian responses at 8.1 mK and 4.9 mK.** The response of a quartz tuning fork at 29.3 bar taken at 8.1 mK (blue) compared to the response at 4.9 mK (red), both obtained after subtraction of the fitted background signal obtained at 8.1 mK (See Supplementary Figure 4c)). The Nyquist plot for the 4.9 mK signal shows an offset from the origin. This is also visible as a negative response for the X signal at 4.9 mK (red) in a).

Because the origin of this shift in background was not evident when the data was being acquired, we introduced a workaround to compensate for this shift. We collect data in a limited period of time (typically 1 day) while ensuring minimal thermal gradient between the thermometer immersed in the ^3He and the quartz fork. In practice, this limits us to temperature sweeps within $\approx 40\%$ of T_c . Following this procedure, we observe an artificial intercept ($Q \neq 0$ at $T = 0$) in

the temperature dependence of the Q in ^3He (Supplementary Figure 6). After subtraction of this intercept ($Q(0)_1$), the inferred Q is plotted as the green line in Supplementary Figure 6. Intercepts of this magnitude or smaller were observed for all the different pressure runs. A list of the offset $Q(0)_1$ values subtracted for each pressure is shown in Supplementary Table 2.



Supplementary Figure 6: Q vs T before and after offsets at $P = 29.3$ bar. Temperature dependence of Q (blue line) inferred following subtraction of the non-resonant signal background. The dashed line is a linear fit on a 10 percent random sample between $1.2T_c$ and $1.4T_c$. The temperature fitting range was kept narrow in order to avoid fitting jumps in the data. After subtraction of the offset, we plot the resulting Q vs T in green.

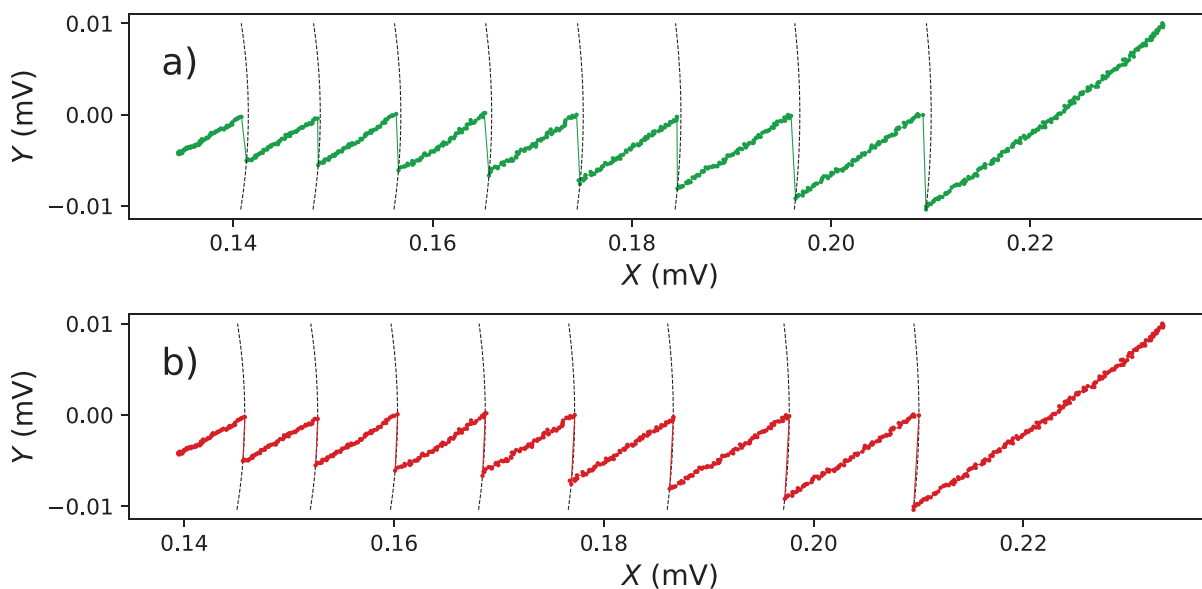
As the ^3He is cooled, due to the increased viscosity, the mass of ^3He coupled to the fork changes, resulting in a decrease of the resonant frequency. Since the PLL operates at a fixed drive

frequency, we reset the drive frequency once $f_D - f_0(T) \geq 5$ Hz. However, because of the offset in X that shifted the Q intercept, Equations 12, 13 are no longer exactly valid. This leads to artificial jumps in the inferred Q produced when the drive frequency is reset (see the insets to Supplementary Figure 6). We note that it was difficult to calculate a line of best fit for linear data broken up into slightly offset line segments as seen in Supplementary Figure 6. This was remedied after the Q continuity correction.

A line was fitted to the $Q(T)$ data, and the $Q(0)_1$ value was converted to a voltage, X_{offset} . The $Q(0)_1$ values vary between $-1 < Q < 6$ with pressure and are listed in Supplementary Table 2. After subtracting the X_{offset} from the raw fork response, we carry out the corrections to achieve the continuity of Q as described next.

In Supplementary Figure 7 (a), we plot the values of $X(T)$, $Y(T)$ obtained during a cooldown at 29.3 bar. The traces are broken up into segments of data collected at a fixed drive frequency. At each transition the drive frequency was reset by the PLL to be on resonance ($Y(T) = 0$). In the top panel of Supplementary Figure 7, at each point where a frequency reset is triggered, a circular arc is traced. This arc of constant Q corresponds to a segment of a Nyquist plot for a circle of diameter corresponding to the inferred Q factor just before the reset, centered at (X, Y) corresponding to $Q/2, 0$. After the frequency reset, the green trace corresponding to the uncorrected data, systematically deviates away from the arc. This indicates that the background fit used has a small systematic frequency dependent error that was not resolved in the fitting procedure described earlier to obtain the Lorentzian fit shown in Supplementary Figure 4. To correct for this offset, the next segment

of the data is shifted to the preceding arc of constant Q . For the specific case of the 29.3 bar data shown here, each segment was shifted by a positive increment to X , corresponding to a positive shift in Q . We find that the individual changes to $\overline{\Delta Q_1}$ are of order 0.2 ± 0.1 . The resulting corrected trace is shown in red in the bottom panel of Supplementary Figure 7. This concludes the first iterative correction.



Supplementary Figure 7: **Nyquist trace during a cooldown at $P = 29.3$ bar.** The top trace shows the observed trace of $Y(T)$ vs $X(T)$ data taken while cooling before correction (green). As the temperature decreases, the $X(T)$ decreases, and $Y(T)$ also decreases corresponding to a decrease in the resonant frequency. Also shown are individual segments of circles (Nyquist plots) originating at $X = 0, Y = 0$ that pass through the last point in $X(T), Y(T)$ before the frequency is reset. The lower panel depicts the trace (red) of $X(T)$ vs $Y(T)$ after adjustment described in the text.

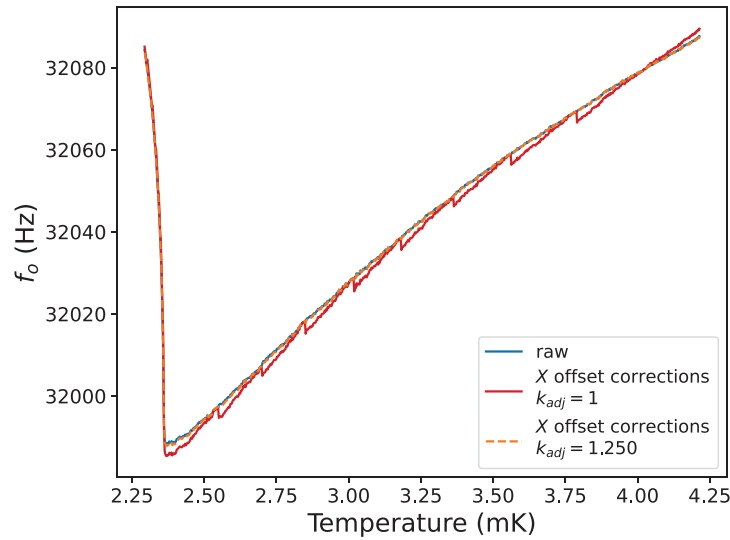
Second and Third Iterative Correction.

Because of the cumulative change in the Q accompanying each reset of the drive frequency, the $T = 0$ intercept seen in Supplementary Figure 3 would be changed. Therefore, a further two iterations to obtain the offsets $Q(0)_2$ and $Q(0)_3$ and Q continuity corrections yielding $\overline{\Delta Q_2}$, $\overline{\Delta Q_3}$ were carried out to minimize the $T = 0$ intercept and any remaining discontinuities in Q across resets of drive frequency. These linear fits were extended to between $1.2 T_c$ and $2T_c$ (or the highest temperature that data at a given pressure was acquired at). The final corrected data and linear fit is shown as the color coded trace in Figure 1 of the main paper, and was used in all further analysis detailed in the main paper. The values for $Q(0)_2$, $Q(0)_3$ and $\overline{\Delta Q_2}$, $\overline{\Delta Q_3}$ are listed in Supplementary Table 2.

Correction to k .

The frequency dependent correction described in the previous sections is essentially confined to $X(T)$. Consequently, the raw inferred resonance frequency $f_0(T)$ is continuous with temperature (blue trace in Supplementary Figure 8). However, after making corrections to the X component of the response as detailed in this Supplementary Note, the inferred frequency is no longer continuous across changes in drive frequency (red trace in Supplementary Figure 8). A correction is needed to k (the difference in the value of the inferred frequency from the drive frequency depends on the value of k - See Supplementary Equations 12, 13). Note that $Y(T) \ll X(T)$, so that $Q(T) \approx X(T) \times k$. Therefore, we apply a multiplicative constant $k_{adj} = k'/k$, where k' is the new voltage to Q conversion factor. The k_{adj} is found by minimizing the sum of all the jumps at a frequency reset,

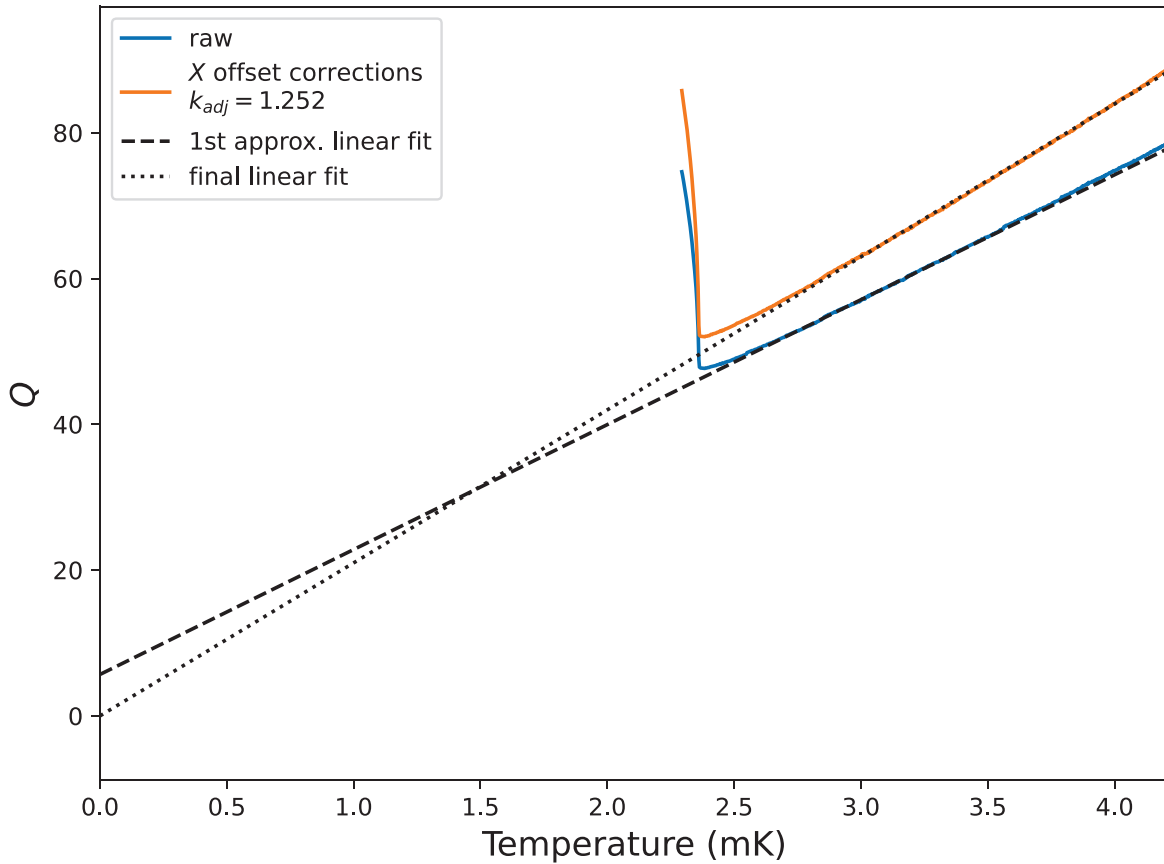
resulting in the dashed orange trace in Supplementary Figure 8 that aligns well the raw resonance frequency. In a few runs (8 bar, 5 bar and 2 bar) the drive frequency was held fixed throughout the temperature sweep. Consequently, there are no values for $\overline{\Delta Q_1}, \overline{\Delta Q_2}, \overline{\Delta Q_3}$ in the table. In these runs, the zero temperature offset was subtracted, and the k_{adj} was found by minimizing the difference in the original raw f_o and the f_o upon a X offset subtraction based on a zero temperature intercept.



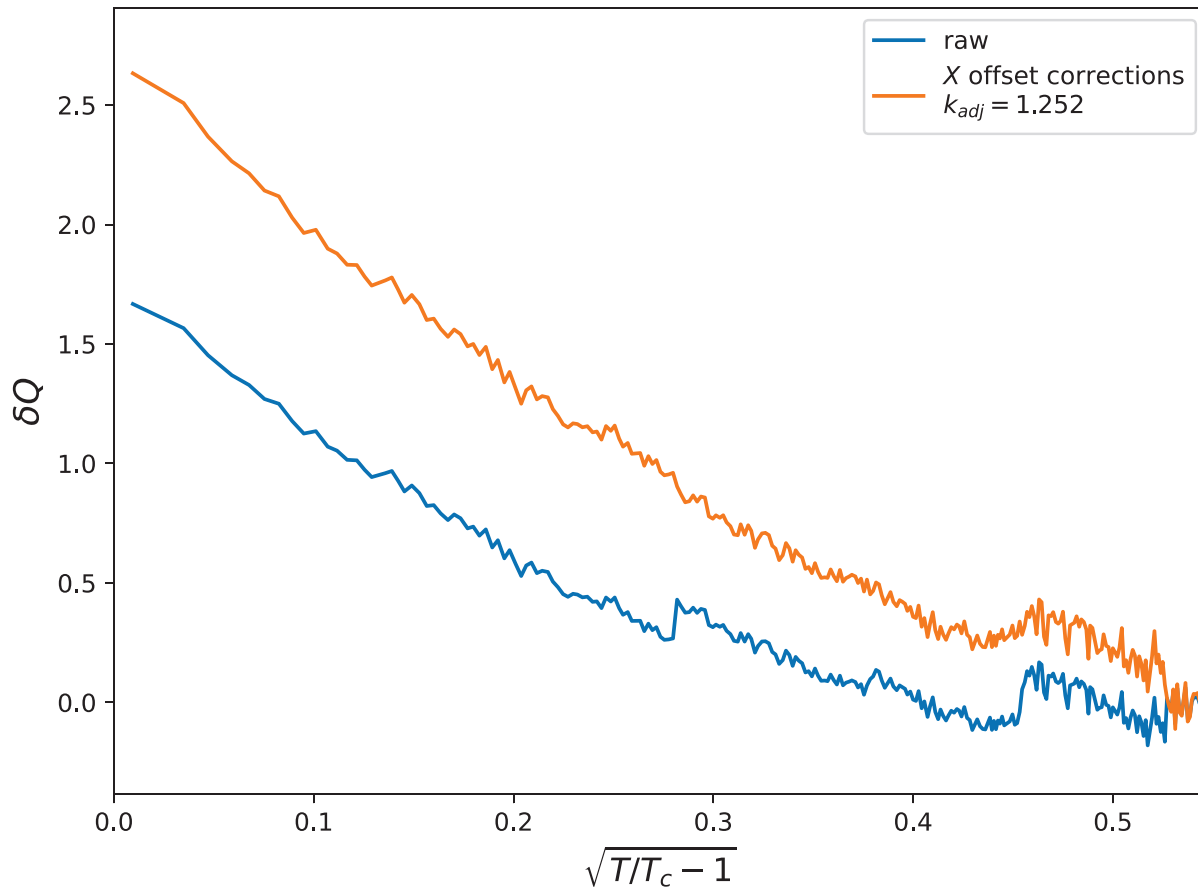
Supplementary Figure 8: **Resonant Frequency vs Temperature at $P = 29.3$ bar.** The blue trace shows the raw data for resonant frequency plotted against the temperature, obtained from the fit to Q at 8.1 mK. Following offsets of Q , the resulting plot (orange) displays discontinuities. This is resolved by appropriate changes to k_{adj} restoring $f_o(T)$ (dashed red line) to the original values.

After following these steps, we plot the corrected results for Q vs T and δQ vs T alongside the uncorrected raw data in Supplementary Figures 9, 10. We also show the full extent of all

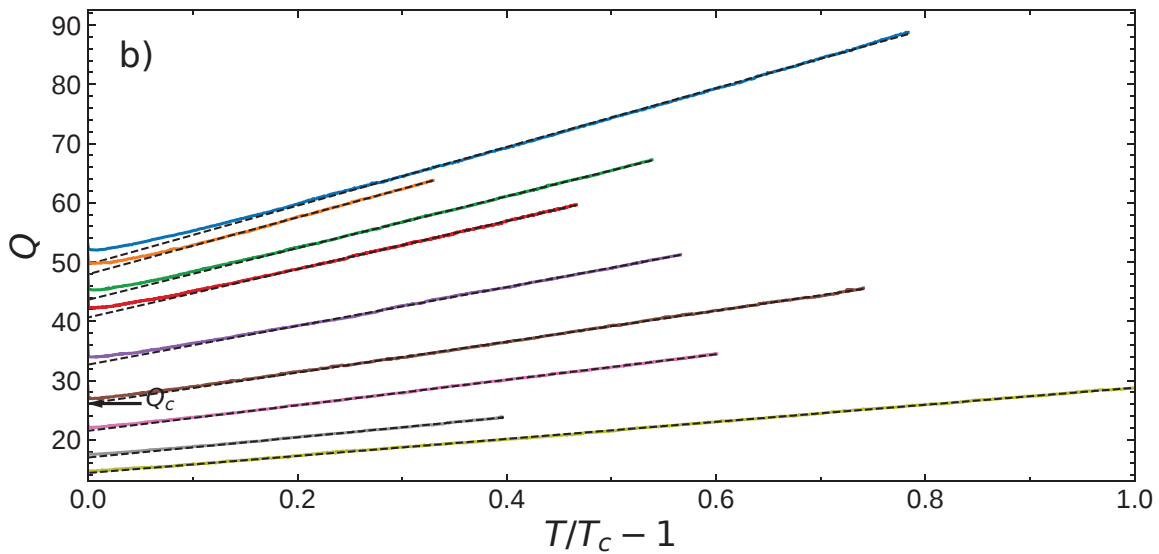
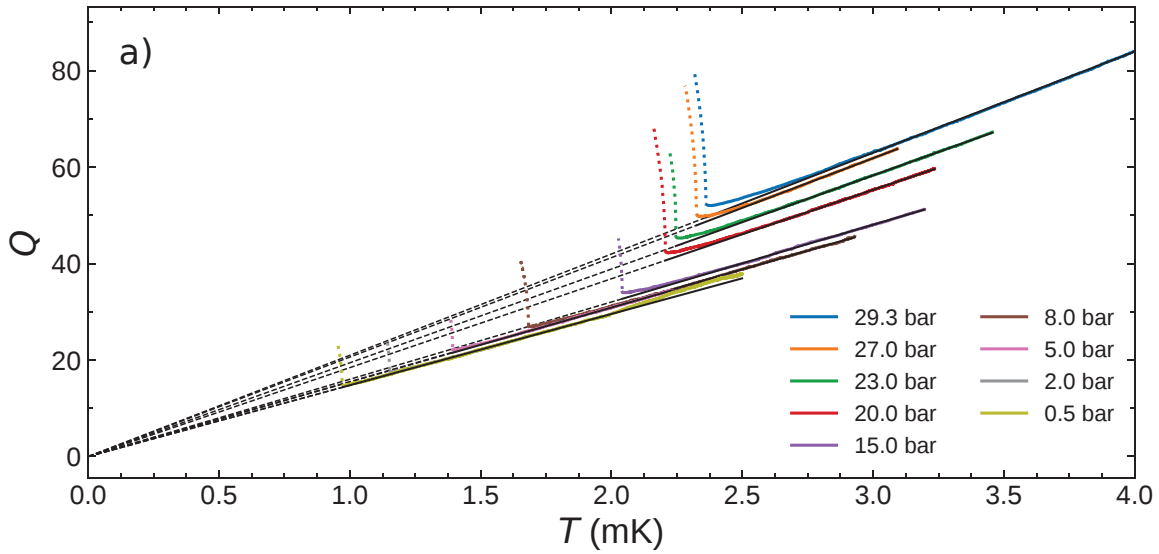
temperatures and pressures measured with corrections applied in Supplementary Figure 11. Individual plots similar to Supplementary Figure 9 for 27 bar, 23 bar, 20 bar and 15 bar are shown in Supplementary Figure 12 and for 8 bar, 5 bar, 2 bar and 0.5 bar are shown in Supplementary Figure 13.



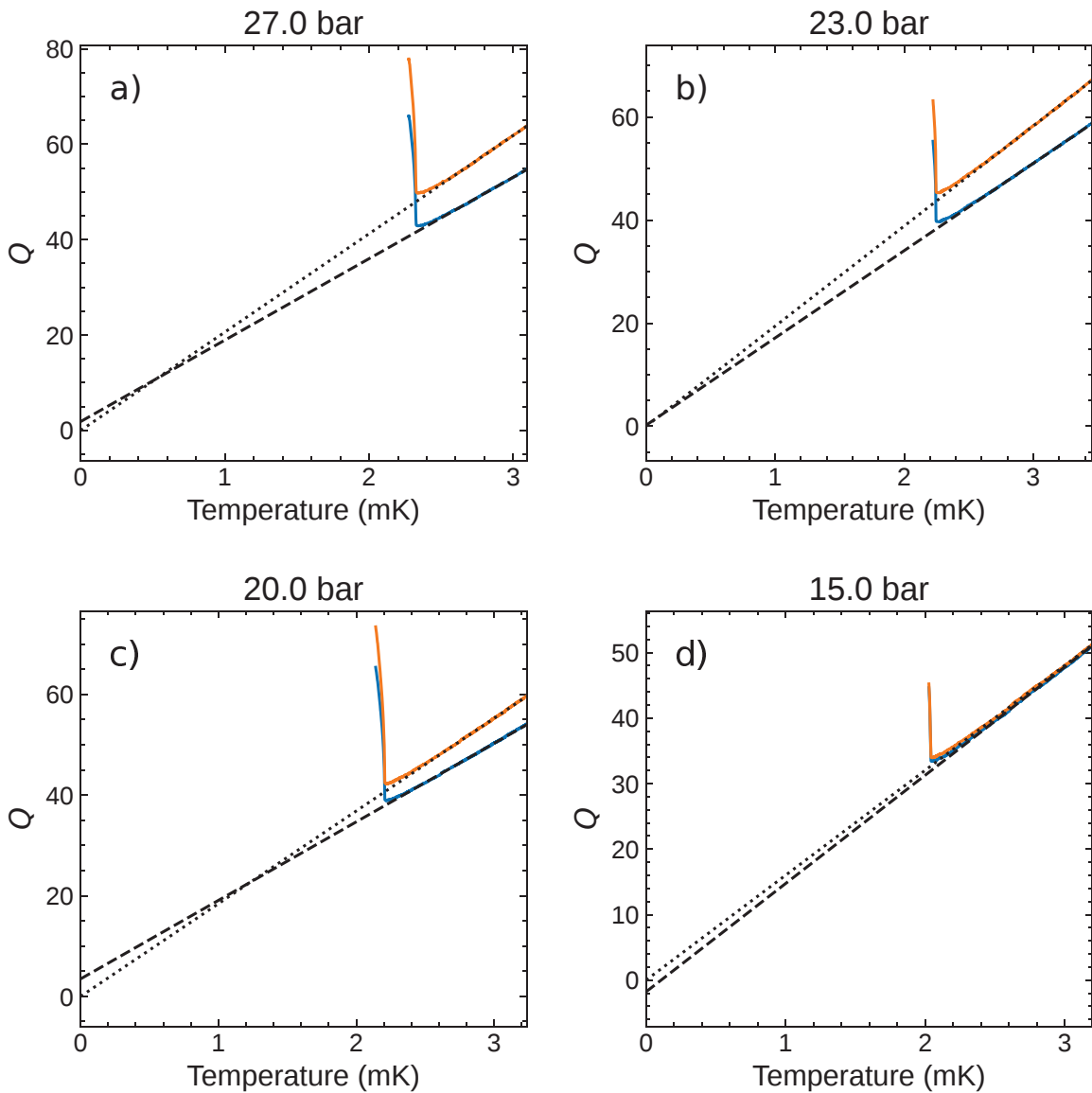
Supplementary Figure 9: Q vs. **Temperature before and after X offset corrections** $P = 29.3$ **bar**. We show the Q before (blue) and after (orange) the X offset and k correction were applied. The plot is shown in gold here appears in Fig 1 a) of the main paper. The dashed line is a linear fit on the raw data in the 1st iteration of the correction procedure. The dotted line is a linear fit on the fully corrected data.



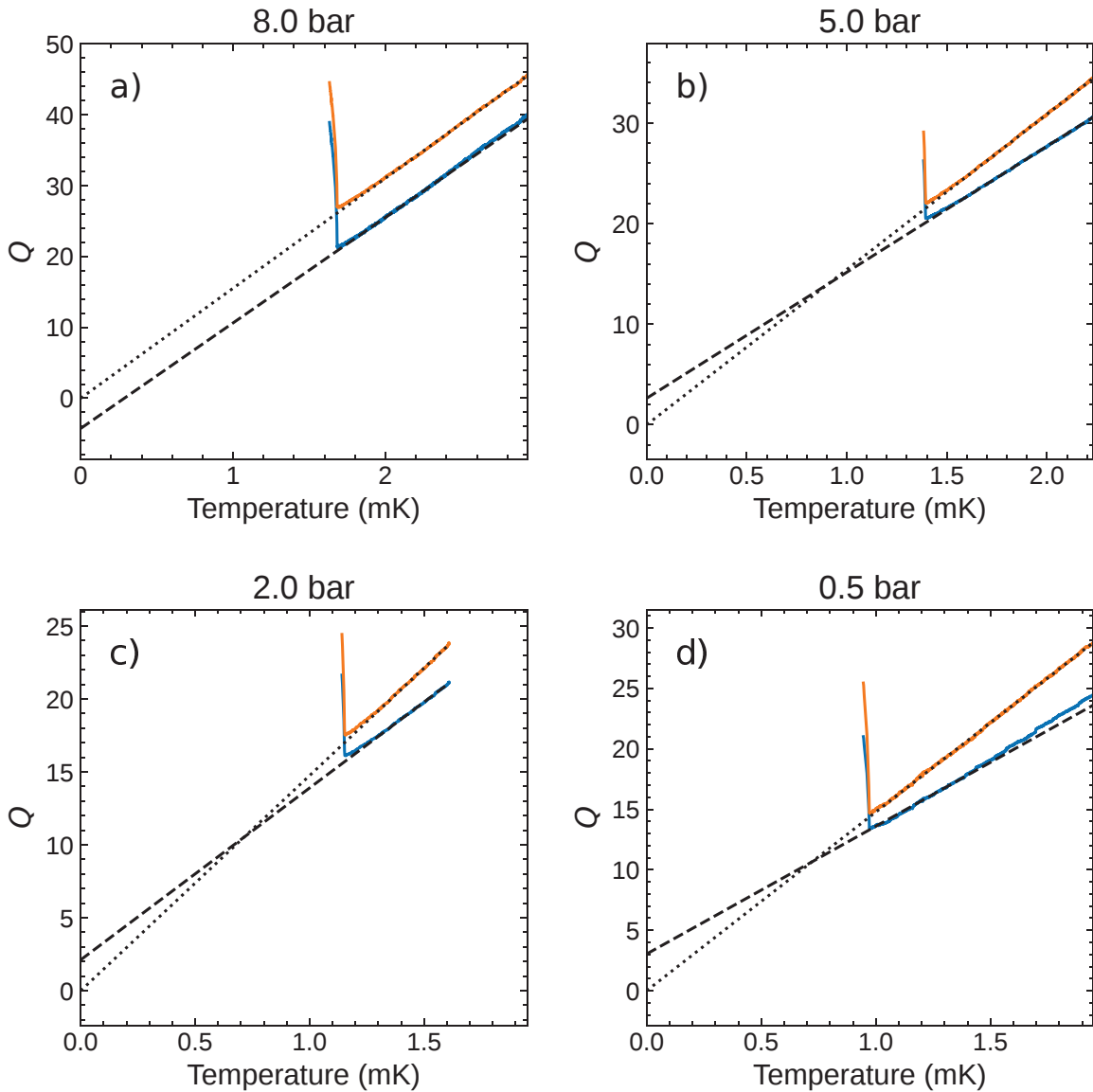
Supplementary Figure 10: δQ vs. **the square root of the reduced temperature before and after offsets at $P = 29.3$ bar.** We show the δQ before (blue) and after (gold) the correction offsets were applied. The plot in shown in gold here appears in Figure 2a) of the main paper.



Supplementary Figure 11: **Corrected Q vs. temperature of all pressures over a larger temperature range.** We show the corrected Q vs. temperature data up to the highest temperature data was taken for each pressure. a) Corrected Q vs temperature, where the dashed lines are linear fits. The dotted colored line is the fork response below T_c . The dashed black lines are the linear fits extrapolated below T_c . b) Q versus a reduced temperature scale.



Supplementary Figure 12: **Corrected Q vs. temperature for a) 27 bar, b) 23 bar, c) 20 bar, and d) 15 bar.** The legend for the traces plotted in each section of the grid are equivalent to Supplementary Figure 9. The plot compares the corrected data (orange), to the “as collected” data (blue). The k_{adj} constants for each run can be found in table 2. The dashed line is a linear fit to the uncorrected data, and the dotted line is the final linear fit to the corrected data.

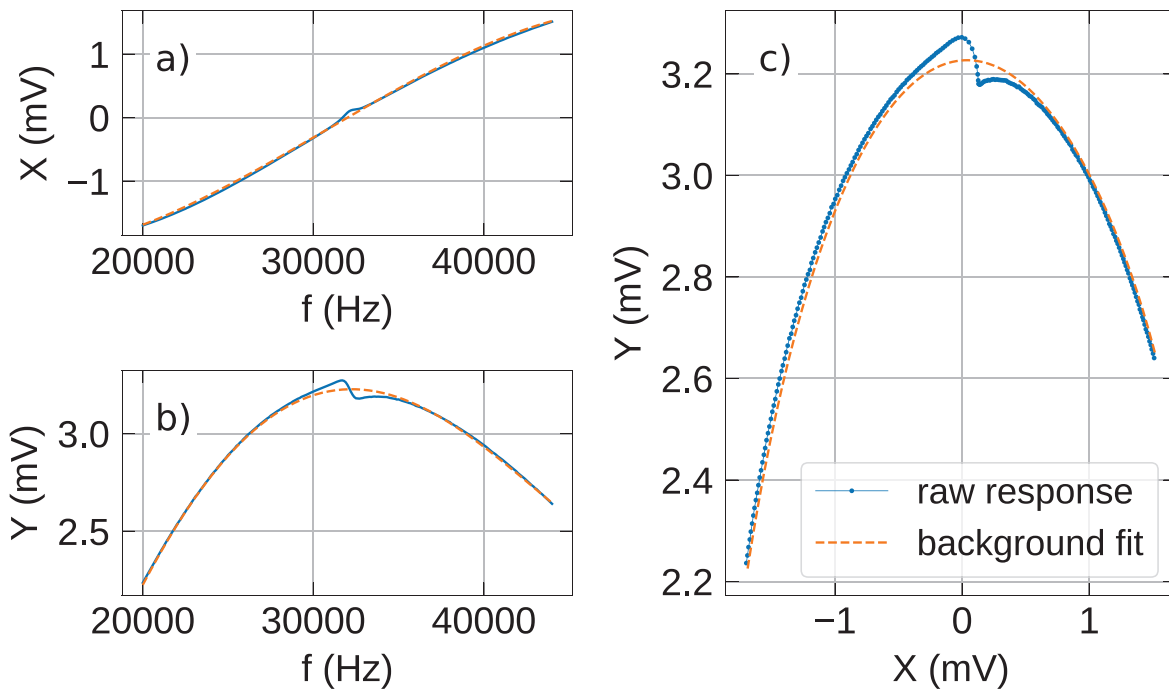


Supplementary Figure 13: **Corrected Q vs. temperature for a) 8 bar, b) 5 bar, c) 2 bar, and d) 0.5 bar.** The legend for the traces plotted in each section of the grid are equivalent to Supplementary Figure 9. The plot compares the corrected data (orange), to the “as collected” data (blue). The k_{adj} constants for each run can be found in table 2. The dashed line is a linear fit to the uncorrected data, and the dotted line is the final linear fit to the corrected data.

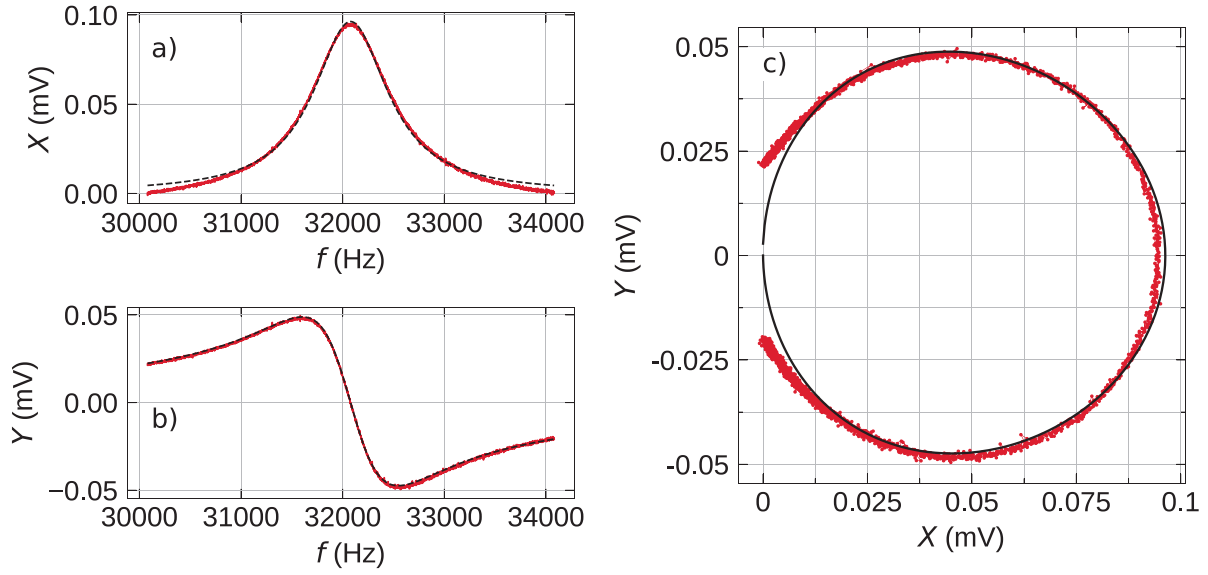
P (bar)	final $Q(0)$	k_{adj}	$Q(0)_1$	$Q(0)_2$	$Q(0)_3$	1st $\overline{\Delta Q_1}$	$\overline{\Delta Q_2}$	$\overline{\Delta Q_3}$
29.3	0.00252	1.25	5.69	1.95	0.059	-0.231	-0.0025	-0.000103
27	4.13e-05	1.22	1.86	0.594	0.00431	-0.00353	-9.13e-05	-7.53e-07
23	-1.3e-05	1.14	0.208	-0.182	-0.00154	-0.00112	3.32e-05	2.23e-07
20	-3.81e-05	1.18	3.48	-0.0172	-0.00146	-0.0829	0.00019	1.35e-06
15	0.000169	1	-1.78	1.47	0.0157	-0.024	-0.000407	-4.22e-06
8	-1.03e-07	1	-4.26	-1.36	9.78e-06	0	0	0
5	0.000111	1.23	2.63	0.0485	-0.00209	0	0	0
2	-5.64e-05	1.25	2.12	-0.0543	0.00154	0	0	0
0.5	2.64e-05	1.42	3.04	0.0837	-0.00319	0.0696	-0.00018	9.17e-07

Table 2: **Supplementary Table 2: Background Subtraction.** The table lists the pressures, the final value of $Q(T = 0)$, the adjusted value of k (the multiplicative factor applied the conversion factor k from signal amplitude to Q), the $Q(T = 0)$ for three iterations of the correction procedure, and the the average jump in Q after a frequency reset for three iterations.

Background in the low- Q regime



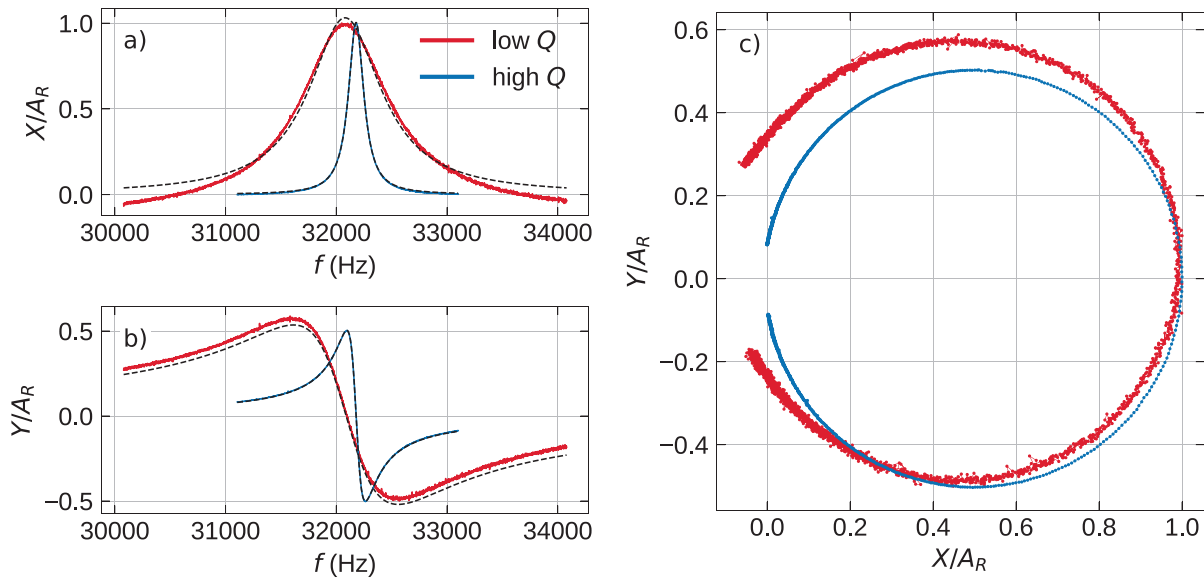
Supplementary Figure 14: **Background subtraction over a wide frequency range in the low Q regime.** $T = 2.5$ mK and $P = 0.56$ bar. a) The X response of the quartz fork fitted to a 3rd order polynomial. b) The Y response of the quartz fork fitted to a 4th order polynomial. c) The fork response over a wide frequency range in a Nyquist plot, together with the fit (orange dashed line).



Supplementary Figure 15: **Background subtraction over a narrow frequency range in the low Q regime.** $T = 2.5$ mK and $P = 0.56$ bar. The Q -factor from this fit is ≈ 35 , and the fitted resonance is $f_0 = 32079$ Hz (linewidth, $\Delta f = 916$ Hz). a) The X response of the quartz fork fitted to the real part of a complex Lorentzian. b) The Y response of the quartz fork fitted to the imaginary part of a complex Lorentzian. c) The quartz fork response and fit in a Nyquist plot.

In addition to the background presented in Supplementary Figures 3, 4, we carried out a frequency sweep to fit the background at low temperature and low pressure. Supplementary Figure 15a) shows poor agreement between the real response and the fit to a Lorentzian. The fit deviation in the X component is observed in the Nyquist plot in Supplementary Figure 15 a) and c) as well. The fork's response is small in the low- Q regime. The broader response due to the low Q and a temperature dependent background, is responsible for a poor fit. In Supplementary Figure 16 we

show the consequence of using a high temperature and high pressure fit to data obtained in the low Q regime.



Supplementary Figure 16: **Low Q sweep with a high Q /high temperature and pressure background.** The blue trace is the response from Supplementary figure 4 minus the background obtained from the wide response in figure 3, at $T = 8.1$ mK and $P = 29.3$ bar. The red trace is the fork response at $T = 2.5$ mK, $P = 0.56$ bar, minus the same high temperature and high pressure background as the blue trace. a) The X responses of the quartz fork fitted to the real part of a complex Lorentzian, and normalized by the resonant amplitude. b) The Y responses of the quartz fork fitted to the imaginary part of a complex Lorentzian and normalized by the resonant amplitude. c) The quartz fork responses in a Nyquist plot normalized by the resonant amplitude.

- [S1] Parpia, J. M., Sandiford, D. J., Berthold, J. E. & Reppy, J. D. Viscosity of normal and superfluid helium three. *J. Phys. Colloques C6* **39**, C6–35–C6–36 (1978). URL <https://doi.org/10.1051/jphyscol:1978617>.
- [S2] Parpia, J. *The Viscosity of Normal and Superfluid ^3He* . Ph.D. thesis, Cornell University (1979).
- [S3] Rusby, R. *et al.* Realization of the ^3He Melting Pressure Scale, PLTS-2000. *J. Low Temp. Phys.* **149**, 156–175 (2007). URL <https://doi.org/10.1007/s10909-007-9502-y>.
- [S4] Tian, Y., Smith, E. N. & Parpia, J. Conversion between ^3He melting curve scales below 100 mk. *Journal of Low Temperature Physics* **184**, 1573–7357 (2022). URL <https://doi.org/10.1007/s10909-022-02721-z>.
- [S5] Greywall, D. ^3He specific heat and thermometry at millikelvin temperatures. *Phys. Rev. B* **33**, 7520–7538 (1986). URL <http://dx.doi.org/10.1103/PhysRevB.33.7520>.
- [S6] Greywall, D. S. Specific heat of normal liquid ^3He . *Phys. Rev. B* **27**, 2747–2766 (1983). URL <https://link.aps.org/doi/10.1103/PhysRevB.27.2747>.
- [S7] Abel, W. R., Anderson, A. C. & Wheatley, J. C. Propagation of zero sound in liquid ^3He at low temperatures. *Phys. Rev. Lett.* **17**, 74–78 (1966). URL <https://link.aps.org/doi/10.1103/PhysRevLett.17.74>.
- [S8] Morley, G. W. *et al.* Torsion pendulum for the study of thin ^3He

films. *Journal of Low Temperature Physics* **126**, 557–562 (2002). URL

<https://doi.org/10.1023/A:1013767117903>.